Renewable Energy 239 (2025) 121967

Contents lists available at ScienceDirect

Renewable Energy

journal homepage: www.elsevier.com/locate/renene

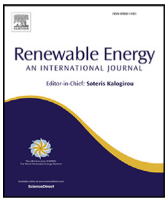

High-resolution working layouts and time series for renewable energy generation in Europe

Oliver Grothe, Fabian Kächele, Mira Wälde *

Karlsruhe Institute of Technology (KIT), Institute for Operations Research, Karlsruhe, 76131, Germany

ARTICLE INFO

Dataset link: https://github.com/MWaterm/High-Resolution-Working-Layouts-and-Time-Series-for-Renewable-Energy-Generation-in-Europe, https://doi.org/10.6084/m9.figshare.22439254

Keywords:
Renewable energy capacity layout
Renewable generation
Weather-to-energy conversion
Solar power
Wind power
Electricity grid

ABSTRACT

The stability and manageability of power systems with a growing share of renewable energies depend on accurate forecasts and feed-in information. This study provides synthetic wind and solar power generation time series for approximately 1,500 European transmission nodes in hourly resolution from 2019 to 2022, along with data-driven layouts of renewable generator allocations. To create these time series and layouts, we develop weather-to-energy conversions using high-resolution weather data. Based on the conversions and elastic-net optimisation, the layouts, which we refer to as *working layouts*, represent a theoretical allocation of generators within each country that produces the current (or alternatively any historical) observed energy output characteristics based on the weather data. This work provides the necessary code to update and adapt layouts and time series for use in custom applications.

1. Introduction

To reduce net greenhouse gas emissions, the EU, like most countries worldwide, is expanding renewable energy generation capacities [1,2]. The energy system, which has so far been based on conventional and centralised electricity generation, transforms into a decentralised system dependent on generators with high weather-conditional variability [3–7]. Because of this, the integration of renewable energy sources poses challenges for the electricity market, including the need for detailed information and accurate forecasts of feed-in from individual generators as well as on different aggregation levels. The interconnection of the European power grids and the impact of weather on renewable energy output also calls for merged data sets of installed capacities and feed-in on a large-scale, i.e., covering the entire continent [8]. However, actual feed-in data sets are often not publicly available, and even the sole information on the spatial allocation of installed renewable generation capacity is only available with a time lag, if at all. In this paper, we, therefore, derive high spatial resolution hourly wind and solar feed-in time series calculated from weather data for mainland Europe. We also provide working layouts with an estimated, realistic allocation of installed wind and solar capacities across the continent. The data set has been generated with great methodical care. Users may update it at any time using our code with the flexibility to limit their analysis to the regions or aggregation levels that interest them.

Calculating feed-in of renewable energy sources is not new to the existing literature. For example, researchers use statistical methods and calculate or predict the feed-in by time series models and deep learning [see, e.g., 9–16]. A comprehensive overview of very short-term forecasting wind and solar generation is provided by [17], whereas [18–20] focus on deep-learning methods for short-term forecasting solar irradiance and PV power of single solar panels and PV systems. [21] investigate regional PV power forecasting in six Italian bidding zones over a year, evaluating the dependency of forecast accuracy. Detailed reviews concerning solar generation forecasting are given by [18,22–24], and wind generation forecasting by [25,26]. Other works directly use weather data for weather-to-energy conversion techniques trained on historical data. Thus, instead of time-series approaches, they develop physical models like also we do, at least partly in this paper. A short overview of the calculation of feed-in data from weather data is provided by [27] (see also the references therein). Studies using weather-to-energy conversions to calculate the generation of renewable energy sources can be found, for example, in [28–35] for wind and in [36–41] for solar.

Approaches that rely on weather-to-energy conversion require detailed data on the locations and specifics of the installed turbines and

---

* Corresponding author.
E-mail address: mira.watermeyer@partner.kit.edu (M. Wälde).
URL: https://www.as.ior.kit.edu/ (M. Wälde).

https://doi.org/10.1016/j.renene.2024.121967
Received 1 April 2023; Received in revised form 15 October 2024; Accepted 20 November 2024
Available online 4 December 2024

solar panels, which are often not publicly available for macro-scale regions due to economic interests and high administrative burdens, as stated above. Researchers have therefore tried to circumvent this lack of data by using layouts only for specific regions or countries, such as Germany or Denmark, where information is publicly available (see, e.g., [42–44]). Additionally, [45] used layouts based on site attractiveness and policy targets to calculate possible trajectories of wind and solar power generation depending on the future share of renewables in electricity generation and other supply and demand factors, and [46] generated forecasts based on the government's expansion plans and targets. The web application Renewables.ninja [47] provides high-resolution, globally accessible data on wind and photovoltaic (PV) generation for the time period 1980 til 2019, based on historical, hourly weather data. Therefore, [28,40] simulate wind and solar generation using models for wind speeds and solar irradiance and based on the reanalysis data set MERRA [48], accounting for factors like turbine specifications, panel tilt, and system losses. The generation data is given relative to installed capacity, so installed capacity data must be available to calculate point-wise or nationwide feed-in.

Another option is chosen by [49], who assumed wind and solar generators to be uniformly distributed over mainland Europe for a first layout and proportionally distributed to the population for a second layout. By doing so, they come up with a comprehensive data set for a European electricity system. However, due to their strong assumptions on the spatial distribution of generators, [49] did not intend the estimated hourly feed-in of these layouts to actually conform to the observed feed-in.

In contrast, we develop synthetic yet realistic capacity layouts for renewable energy generation plants in our paper. The provided layouts are learned from observed data, have a high spatial resolution, and result in a comprehensive and precise data set for the feed-in of renewable energy sources. We focus on wind and PV energy, as these have the largest share of renewable generation capacity and exhibit a high degree of weather dependency. We provide information on potential installed wind, onshore and offshore, and PV capacities as well as on the feed-in generated with these capacities scaled to the network nodes of the main continental European transmission network. The estimated layouts are derived as follows. We convert high-resolution numerical weather data into energy signals using physical models of the power curves from wind turbines and solar modules. Hereby, we carefully consider parameters like the wind conditions at hub height, the sun's incidence angle on the solar panels as well as the weather-dependent proportions of direct and diffuse irradiation. Resulting energy signals are then mapped to 1494 main nodes of the European transmission network to form synthetic power outputs. We next use the synthetic outputs to explain actual measured wind and solar feed-in with an elastic-net regression approach and come up with an estimate of installed wind and solar capacities at each node, which builds our *working layout* for renewable energy sources in mainland Europe. We show that using our working layouts in weather-to-energy conversion approaches leads to precise estimates of the actual electricity feed-in. Further, the working layouts inherit most of the characteristics of the true layouts for places where the true layout is known. Thus, the layouts can be used to map and forecast the generated feed-in in the European transmission network. Finally, we use our layouts to create a comprehensive data set for mainland Europe, including the hourly resolution wind, onshore and offshore, and PV power generation from 2019 to 2022 and high-resolution layouts of installed wind and PV capacities. By making the code publicly available, we enable others to generate results for a specific time horizon and tailor them to their needs. Additionally, we provide a detailed methodology for converting weather data to wind and especially to solar generation, filling a gap in previous research by providing a comprehensive understanding of this conversion process and the required variables.

The remainder of the paper is structured as follows. First, the data used in our approach are presented in Section 2. In Section 3, we explain the layout generation step-by-step, including a detailed description of the weather-to-energy conversion, the cell-to-node allocation and the layout estimation. Section 4 presents the results of this paper. It contains the results and evaluations of the layout and the feed-in data sets. We conclude in Section 5.

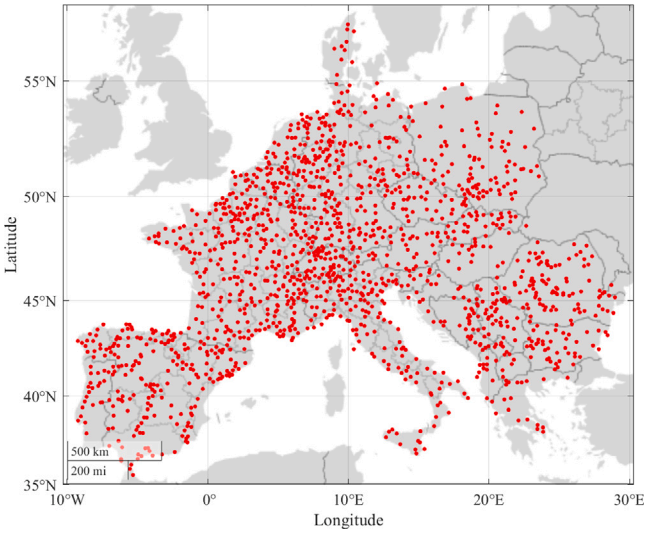

Fig. 1. Nodes of the European transmission network marked in red.

Table 1
Countries in the European transmission network used in this study.

Country	Abbreviation
Albania	ALB
Austria	AUT
Belgium	BEL
Bulgaria	BGR
Bosnia Herzegovina	BIH
Switzerland	CHE
Czechia	CZE
Germany	DEU
Denmark	DNK
Spain	ESP
France	FRA
Greece	GRC
Croatia	HRV
Hungary	HUN
Italy	ITA
Luxembourg	LUX
North Macedonia	MKD
Montenegro	MNE
Netherlands	NLD
Poland	POL
Portugal	POR
Romania	ROU
Serbia	SRB
Slovakia	SVK
Slovenia	SVN

2. Data

Our analysis is based on high-resolution historical weather data and the main continental European transmission network nodes. The nodes belong to a network model which comprises 1.494 buses, shown in Fig. 1. It is based on the ENTSO-E grid map and was first developed by [50]. We use the geographical locations of this network, which are transformed by [49] and are available at [51]. The network captures countries of mainland Europe, listed in Table 1.

For the weather data, we use high-resolution historical weather data, i.e., data which is often provided from reanalysis data, where

Table 2
Variables of the ERA5 data set used in this study.

Variable	Naming ERA5	Description
$\approxeq$	100 m u-component of wind	Eastward component of the 100 m wind
$\succapprox$	100 m v-component of wind	Northward component of the 100 m wind
z_0	Forecast surface roughness	Aerodynamic roughness of surface
t_a	2 m temperature	Temperature of air at 2 m above the surface
ρ	Forecast albedo	Reflectivity of the earth's surface
I_{bn}	Total sky direct solar radiation at surface	Amount of direct solar radiation
I_s	Surface solar radiation downwards	Amount of solar radiation that reaches a horizontal plane at the surface of the earth

weather measurements, models and numerical model predictions are combined into one large comprehensive data set. More specifically, our analysis uses the *ERA5 hourly data on single levels from 1959 to present* reanalysis data set [52] for the years 2019 to 2022. Since the data set includes more than 250 variables, we only use an excerpt with the variables given in Table 2 for each location.

The data is accessed via the *Python CDS Toolbox API*.[1] We also use sea depth data extracted from the GEBCO data[2] and match it to the coordinates of the ERA5 data to exclude locations where offshore wind farms are technically not possible or not profitable yet.

Hourly actual feed-in data for every country is provided by the ENTSO-E transparency platform [53]. Note this important point: Since the feed-in and weather data have different accumulation schemes, with the weather data containing accumulated data for the hour ending at the timestamp, and the feed-in data accumulating over the hour following the timestamp, it is necessary to align the two data sets with each other. To clarify, the 10 a.m. timestamp, for example, refers to 10 a.m. to 11 a.m. in the feed-in data and to 9 a.m. to 10 a.m. in the weather data; thus, we shift the timestamps in the feed-in data by one hour.

To assess the synthetic working layouts, the synthetic feed-in data is compared with both the actual hourly feed-in data and the feed-in data from the Renewables.ninja web application for 2019 [47]. Therefore, the relative Renewables.ninja generation data needs to be multiplied by the installed capacity of each respective country, which we obtain in line with the approach from the ENTSO-E transparency platform [53].

3. Methodology

Our approach is based on comparing synthetic energy signals with the actual feed-in of renewable energy sources. From a high level, we first calculate the nominal power from solar and wind power generators in each weather cell of the ERA5 data set for each hour. Then, each weather cell is assigned to a transmission node within the European electricity grid structure, where we aggregate the information from multiple weather cells. Third, we facilitate an elastic-net regression approach to estimate the number of renewable generators at each transmission node. The installed capacities are then given by the estimated number of renewable generators multiplied by the rated power of the exemplary used generators. The resulting layout information can be used to improve forecasts, enhance grid stability or define expansion goals for renewable energies. In the following, we first discuss the calculation of nominal power for each weather cell and then introduce the weather cell combination and the estimation approach. Readers which are experts in weather-to-energy conversion can skip Section 3.1, where we explain this step in detail.

3.1. Calculation of renewable power generation

We calculate the generated power based on historical weather data and the technical specifications of the used renewable generators. More precisely, we transform the measured solar radiation and wind speeds to nominal power outputs for each weather cell. The transformation is done using the technical specifications of state-of-the-art solar panels and wind turbines. We first consider the calculation of solar power generation followed by wind power generation, onshore and offshore.

Solar

To calculate the nominal power generated by solar panels, it is important to consider both solar radiation and temperature. Solar radiation consists of direct, diffuse, and ground-reflected components, all of which must be taken into account. In the ERA5 data set, the variable *Surface solar radiation downwards* (denoted as I_s) represents the total amount of solar radiation that a pyranometer would measure, including both direct and diffuse radiation. To separate these components, we subtract the direct radiation component given in the variable *Total sky direct solar radiation at surface* (denoted as I_{bn}). We then calculate the ground-reflected component using the *Forecast albedo* variable (denoted as ρ), which measures the Earth's surface reflectivity. Since radiation is measured in Joule per square meter ($[\mathrm{J/m^2}]$), we convert it to Watt-hours (Wh) by dividing by 3600. This is because 1 Joule equals 1 Watt-second ($1\ \mathrm{J} = 1\ \mathrm{Ws}$), which is approximately 0.00027777 Watts per m^2 over the course of 1 h.

We now give a compact presentation of the important aspects and formulas for solar conversion. In a nutshell, we first determine the angle of the sun for the given location, time, and date. Then, the actual radiation on the tilted surface of the solar panel is calculated. Third, we use the radiation, ambient temperature, and specifications of the solar panel to determine the cell temperature and, finally, the resulting efficiency. Last, this value is multiplied by the corresponding radiation and discounted for further losses. For more details on the following calculations and formulas, we recommend the excellent books by [54,55].

First, the sun's radiation angle is needed, which depends on the date, time, and geographical location. Since the earth's axis of rotation is inclined at an angle of 23.45° from the ecliptic axis of the earth's rotation around the sun, the polar axis is moving with respect to the sun. Thus, we calculate the angle δ, called *declination*, between the normal of the earth's axis of rotation and the sun's rays for each day first. The declination in radians can be computed by the formula given by [56]

$$\begin{aligned}\delta = {} & 0.006918 - 0.399912 \cdot \cos(\Gamma) + 0.070257 \cdot \sin(\Gamma) \\ & - 0.006758 \cdot \cos(2\Gamma) + 0.000907 \cdot \sin(2\Gamma) \\ & - 0.002697 \cdot \cos(3\Gamma) + 0.00148 \cdot \sin(3\Gamma),\end{aligned} \tag{1}$$

where the *day angle* Γ in radians is given by

$$\Gamma = \frac{2\pi \cdot (N-1)}{365} \tag{2}$$

and N is the day of the year.

Further, we consider the change of declination during the day as constant [see, e.g., 55,57] and adjust it with the *hour angle* h. Since

---

[1] The documentation of the toolbox is available under https://cds.climate.copernicus.eu/toolbox/doc/api.html; accessed 17-01-2023

[2] The data is available under https://download.gebco.net/; accessed 15-12-2022

the earth does a full rotation (i.e., 360°) within 24 h of the day, each hour accounts for a change of ±15° from the solar noon (positive numbers for afternoon hours). The apparent solar time AST, needed for computations, is given by

$$AST = LST + ET \pm 4 \cdot (SLon - LLon),$$

with $SLon$ and $LLon$ being the standard and local longitude to correct for the sun's traverse within a timezone (about 1° in 4 min). There, $SLon$ is a selected meridian near the centre of a timezone. The sign is positive (+) if the location is west of Greenwich and negative (-) otherwise. ET is the *equation of time* accounting for different lengths of the day within the year calculated by

$$ET = 9.87 \cdot \sin(2B) - 7.53 \cdot \cos(B) - \sin(B),$$

where $B = (N - 81) \cdot 360/364$. For the hour angle h in degrees follows

$$h = (AST - 12) \cdot 15. \tag{3}$$

After the adjustments for a date, time and location, we calculate the angle of radiation on a tilted solar panel, the *incidence angle* θ. We denote the *tilt angle* of the panel by β and the *surface azimuth angle*, i.e., the orientation of the panel (westward orientated panel positive), by Z_S. The incidence angle θ in radians is now calculated by

$$\begin{aligned} \cos(\theta) = &\sin(L)\cdot\sin(\delta)\cdot\cos(\beta) - \cos(L)\cdot\sin(\delta)\cdot\sin(\beta)\cdot\cos(Z_s) \\ &+ \cos(L)\cdot\cos(\delta)\cdot\cos(h)\cdot\cos(\beta) \\ &+ \sin(L)\cdot\cos(\delta)\cdot\cos(h)\cdot\sin(\beta)\cdot\cos(Z_S) \\ &+ \cos(\delta)\cdot\sin(h)\cdot\sin(\beta)\cdot\sin(Z_s), \end{aligned} \tag{4}$$

where δ again is the declination of the sun during the day, L the local latitude and h the hour angle, all converted to radians before plugged into the above equation [55,57].[3]

With the radiation angles at hand, we next determine the actual radiation at our solar panel. Therefore, we use the model proposed by [58,59] and adjust the given direct normal radiation I_{bn} (*Total sky direct solar radiation at surface*) such that it is assumed to be perpendicular to the earth's surface by $I_b = I_{bn} \cdot \cos(\phi)$, with ϕ being the *solar zenith angle* in radians calculated using Formula (4) for a tilt angle of $\beta = 0$ and a surface azimuth angle $Z_S = 0$.

The radiation on a tilted surface (i.e., the solar panel) I_t with tilt angle β converted to radians is then calculated by

$$\begin{aligned} I_t = &\underbrace{(I_b + I_d A)R_B}_{\text{Direct radiation contribution}} \\ &+ \underbrace{I_d(1-A)\left(\frac{1-\cos(\beta)}{2}\right)\cdot\left(1+\sqrt{\frac{I_b}{I_b+I_d}}\sin(\beta/2)^3\right)}_{\text{Diffuse radiation contribution}} \\ &+ \underbrace{(I_b+I_d)\rho\left(\frac{1-\cos(\beta)}{2}\right)}_{\text{Reflected radiation contribution}}, \end{aligned} \tag{5}$$

where I_b is the direct radiation, I_d the diffuse radiation, and the last term reflects the ground reflected radiation with ρ being the forecast albedo, i.e., the reflectivity of the Earth's surface. Further, R_B is the *bean radiation tilt factor*, which includes the earlier calculated incidence angle θ and is calculated by $R_B = cos(\theta)/cos(\phi)$, both in radians. Next, A is the anisotropy index defined as $A = I_{bn}/I_{ex}$ where I_{ex} is the extraterrestrial radiation depending on the day of the year N, i.e., $I_{ex} = 1366.1\ \mathrm{W/m^2} \cdot [1 + 0.033 \cdot \cos(360N/365)]$ (see, [54], Section 2).

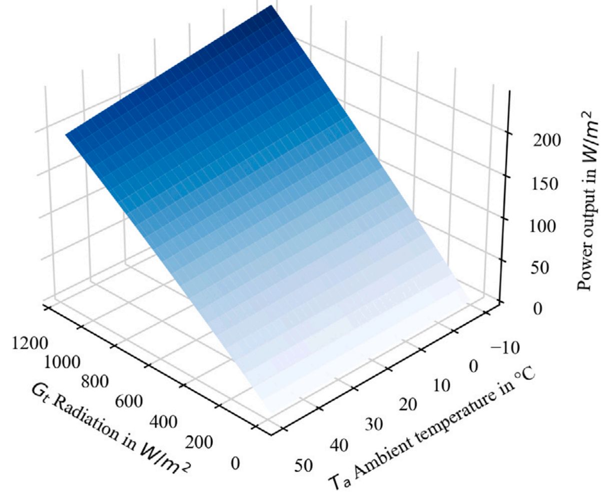

Fig. 2. Power of LongiSolar LR4-72HBD solar panel depending on radiation and cell temperature.

Last, the calculated radiation I_t and the ambient temperature t_a serve as input for the conversion to a power signal. Here we use the *LongiSolar LR4-72HBD* as a benchmark solar cell and leverage its technical characteristics to calculate the corresponding nominal power. It is a rather modern solar cell used in several European solar power plants. The efficiency of the solar panel generally depends on its temperature t_c and the radiation I. To account for both, we start with the efficiency given in the data sheet of the solar panel, the reference efficiency η_r, for testing conditions and correct it iteratively with the estimated cell temperature t_c similar to other authors (cf., Kalogirou [54, Section 9.5]; Durisch et al. [60] or Beyer et al. [61]). The cell temperature t_c is estimated based on radiation I_t, the temperature of the ambient air t_a, and the temperature-related efficiency of the solar panel $\eta_{t_c}(I)$, which we set to the reference efficiency for the first approximation. For the calculation follows

$$t_c(I_t, t_a) = (t_c^{NOCT} - t_a^{NOCT}) \cdot \frac{I_t}{I^{NOCT}} \cdot \left(1 - \frac{\eta_{t_c}}{\xi}\right) + t_a, \tag{6}$$

where super-script $NOCT$ denotes the *Nominal Operating Cell Temperature* and radiation at nominal operating cell temperature given in the data sheet and the transmittance–absorptance product ξ is set to 0.9 to account for reflected energy at the panel [55, Section 23].

Afterwards, the temperature-related efficiency η_{t_c} is updated via

$$\eta_{t_c} = \eta_r + \mu_\eta \left(t_c - t^{NOCT}\right), \tag{7}$$

with the temperature coefficient of maximum power efficiency μ_η calculated by $\mu_\eta = \eta_r \cdot \mu_V / V_{mp}$. There, η_r again denotes the reference efficiency, μ_V the temperature coefficient of open-circuit voltage, and V_{mp} the voltage at maximum power all given in the data sheet of the solar panel [55, Section 23.2]. Formulas (6) and (7) demonstrate the high interdependence between the cell temperature and the actual efficiency of the solar cell. Since the first estimate of the cell temperature is calculated based on the reference efficiency η_r, the estimates of both variables are updated. Therefore, we use the same formulas but now based on the first estimates of both variables to approximate the true values of t_c and η_{t_c}. Thus, the cell temperature t_c is updated with the first estimate of the efficiency η_{t_c} by Formula (6). Afterwards, η_{t_c} is updated a second time using the new value of t_c. This two-step update has shown to be sufficiently precise in simulations and further updates do only account for marginal improvements in precision. We display the resulting power of the solar cell, depending on radiation and cell temperature, in Fig. 2.

In the last step, the calculated efficiency η_{t_c} (Formula (7)) is multiplied by the actual radiation per square meter on the tilted surface I_t, the area of the solar panel S and a discount value of 95% to account for further losses, e.g., the efficiency of the inverter. Converted from

---

[3] Degrees can be converted to radians by multiplying with π and dividing by 180.

the measured unit Watt [W] in [MW], the resulting power p_s emerges to

$$p_s = \left(\eta_e \cdot I_t \cdot S\right)/1000 \cdot 95\%. \tag{8}$$

We use hourly data and assume constant power generation within one hour, so the actual power and the produced energy within the hour measured in [MWh] have the same absolute value. For all calculations, we set the tilt angle $\beta = 45°$ and assumed that 50% of solar panels are installed facing south while 25% are facing westwards and eastwards, respectively. These values have shown to be optimal settings for estimating the data set created in this paper for mainland Europe in previous intensive analyses and reflect the non-optimal conditions in reality.

Remark 3.1. Specific radiation may vary widely within a single grid box/weather cell, depending on clouds or other local characteristics. However, since our goal is to estimate the renewable layout on a regional basis, i.e., on grid nodes, the resolution provided in the ERA5 data (average over each model grid box) is sufficient for our usage.

Wind

Next, we calculate the electricity resulting from wind power generation. To do so, we leverage the wind speeds given in the ERA5 data set [52]. For each weather-cell location, we extract the lateral wind speed components and compute the absolute wind speed v_{100}.

In the subsequent step, these wind speeds in 100 m have to be transformed to the hub height of the used benchmark wind turbine. For the adaption of wind speed to the hub height, we follow [62–64], and assume a logarithmic velocity profile

$$v_{hub} = v_{100} \cdot \left(\frac{log(h_{hub}) - log(z_0)}{log(100) - log(z_0)} \right). \tag{9}$$

Here, z_0 corresponds to the surface roughness depending on the typical landscape, atmospheric conditions or state of the ocean in the weather cell and is provided in the ERA5 data set [52].

Note, that the use of the surface roughness from ERA5 data set for extrapolating wind speeds to turbine hub heights with logarithmic velocity profile is a simplification and may in general be too simplistic in particular for grid points and weather cells in coastal regions. There, surface roughness varies with wind direction, and the assumption of a homogeneous terrain in the logarithmic velocity profile does not hold [65]. Additionally, ERA5 applies orographic drag parametrisation, which affects near-surface winds, especially over complex terrain (see, e.g., [66,67]). A simple logarithmic velocity profile fails to account for these terrain effects (see, e.g., [68]). Given the aim of this paper, which is to provide realistic energy signals for many grid points across Europe, along with joint capacity layouts (both adjustable in the code and updateable by the user), we must focus on simplicity and avoid increased use of computational memory or processing time. Therefore, we choose to accept this simplification and prioritise scalability and applicability over regional precision. An empirical justification for this decision is later provided by the quality of our results, at least for aggregated data, where we can compare with measured energy production. However, if one wanted to improve this part of our approach within the code, the use of direction-dependent surface roughness [65] and more sophisticated terrain models that account for sub-grid scale orography [67] is recommended. More generally, hybrid methods combining observational data, mesoscale models, and data assimilation could further enhance wind speed extrapolations, particularly in complex or coastal regions [68]. These methodological adjustments would improve the accuracy of wind speed projections and the reliability of wind energy resource assessments.

The calculated wind speeds are now transformed to nominal power outputs using the turbine's power curves, i.e., a function that maps the wind speed in [m/s] to power in [MW]. Again, feeding in for an hour with that power leads to produced energy measured in [MWh] of the same absolute value.

We consider two different turbines for onshore and offshore installation. For the onshore component, we use the *Siemens SWT 107* wind turbine with a rated power of 3.6 MW and a hub height of 90 m. For the offshore component, we use the *MHI Vestas V164* with a rated power of 9.5 MW and a hub height of 105 m. We resort to these two frequently used types as reference turbines for all weather cells, which form a cross-section of older and newer turbines with their hub height and rated power. To obtain a functional relationship at each wind speed, we fit a combination of third-order polynomials to the point-wise given nominal power of both turbines [69]. A piece-wise definition of the function resulting in the actual power output p_w is given by

$$p_W(v_h) = \begin{cases} 0, & if\ v_{hub} < v_{min} \\ \alpha_1 v_{hub}^3 + \beta_1 v_{hub}^2 + \gamma_1 v_{hub} + \delta_1, & if\ v_{min} < v_{hub} < v_{split} \\ \alpha_2 v_{hub}^3 + \beta_2 v_{hub}^2 + \gamma_2 v_{hub} + \delta_2, & if\ v_{split} < v_{hub} < v_{rated} \\ p_{rated}, & if\ v_{rated} < v_{hub} < v_{max} \\ 0, & if\ v_{max} < v_{hub}, \end{cases}$$

where v_{hub} is the wind speed at hub height. Further, v_{min} is defined as cut-in speed, i.e., the minimum wind speed required for electricity production, and v_{rated} is the minimum wind speed for the rated power (related to this p_{rated} is the rated power of the wind turbine). At the top end, v_{max} determines the cut-out speed, i.e., the maximum wind speed where the turbine is operated and is set to $v_{max} = 25$ m/s for all turbines. Further, we define v_{split} as the turning point within our functional representation, where we change to the second polynomial. This point is located where the concavity of a fitted third-order polynomial on the power curve changes sign (see [69] for details). The resulting power curves are depicted in Fig. 3. In the following, we denote the actual power of onshore turbines as p_{wl} and offshore generation as p_{wo}.

3.2. *Weather cell combination*

In the previous section, we calculated the nominal power of solar panels and wind turbines in each of the 15,292 weather cells in the ERA5 data set. We now aim to assign each weather cell to one grid node to aggregate the generated power of multiple weather cells to one transmission node. The aggregated power is later used for the estimation of the renewable energy layout by an elastic-net.

We, therefore, first map each weather cell c (thus its renewable generators) to its closest transmission node $n_i,\ i \in \{1, \dots, N\}$, of all N transmission nodes since this connection is the cheapest and most efficient. Further, we filter the resulting allocation and only keep a mapping of a weather cell c to its transmission node n_i if the corresponding distance $d(c, n_i)$ is smaller than the maximal distance between any two adjacent transmission nodes, i.e.,

$$d(c, n_i) \overset{!}{<} d(n_k, n_\ell) \text{ for all } k, \ell = 1, \dots, N.$$

This condition ensures that we only take weather cells with a reasonable distance to the power grid into account, e.g., cells covering the coastal area (used for offshore wind constructions) but not the complete ocean. For the special case where no weather cell is assigned to a transmission node, we assign the closest weather cell to this node as well. Note that this is only the case for 25 nodes in total, thus leading to 25 weather cells which are assigned to two nodes: the node closest to the weather cell and the node for which the weather cell is the closest. Fig. 4 visualises the resulting assignment of all used weather cells (small dots) to the network nodes (fat dots). Weather cells that are assigned to a node are coloured correspondingly. The double-assigned weather cells are colour-coded to their nearest node.

In the last step, the nominal power signals of all weather cells associated with a transmission node are averaged by generator type. To do so, we classify each weather cell depending if it is mainly covering ocean or land. The ocean weather cells are not considered for averaging solar signals, while the land cells are ignored for calculating

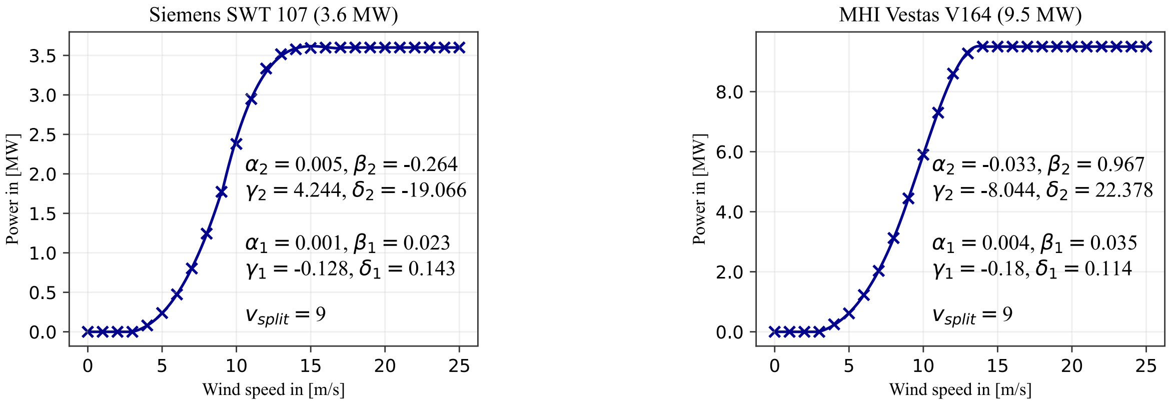

Fig. 3. Power curves Siemens SWT 107 (left) and MHI Vestas V164 (right) with corresponding parameters of the fitted polynomials and change-point v_{split}.

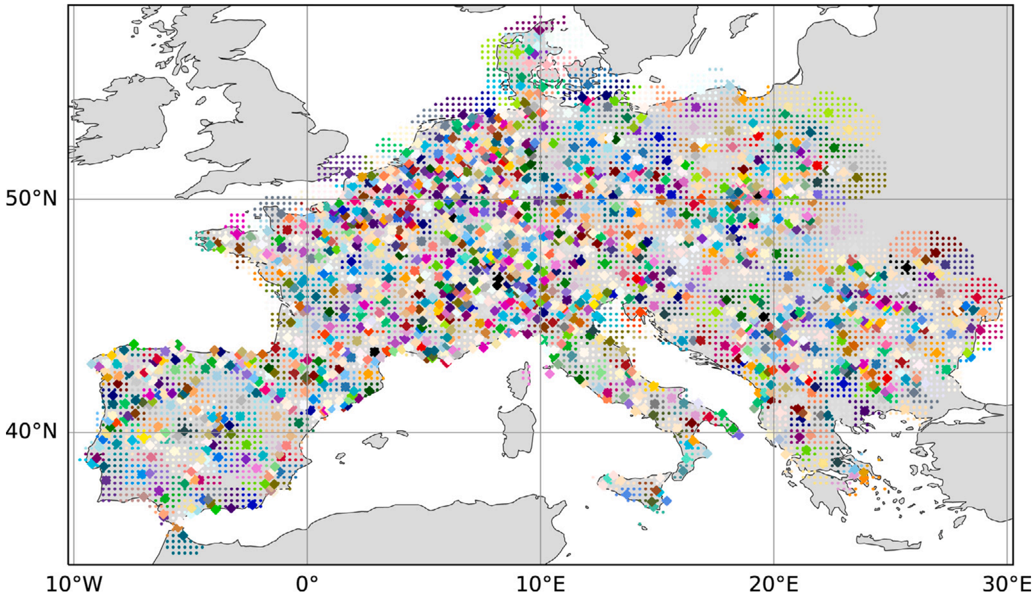

Fig. 4. Nodes of the European transmission network (fat) and assigned weather cells (small) of the ERA5 data set.

the average offshore wind power signals. We distinguish onshore and offshore wind power signals in the same manner and further exclude offshore weather cells with a sea depth $\geq 70\,m$ due to technical and construction restrictions of offshore wind turbines. The result is a power signal for each transmission node, scaled to the nominal power of one representative renewable generator by type.

3.3. Layout estimation

Now, the allocation and, thus, the working layouts of renewable energy generators across Europe are estimated from derived power signals per transmission node and actual feed-in data of solar and wind power. The actual generation data for onshore wind power in_{wl}, offshore wind power in_{wo}, and solar in_s is openly available on a country level at the ENTSO-E transparency platform for the years 2019 to 2022 [53]. For the estimation, we facilitate the condition that the total feed-in of wind and solar power has to be the sum of the produced power at all transmission nodes, i.e., the power signal of a single solar cell or wind turbine multiplied by the number of installed generators, at country-based resolution for each hour. Thus the feed-in in_s, in_{wl} and in_{wo} for each country at any time-step $t = 1, \dots, T$ is given by

$$in_s = \sum_{n=1}^{N} w_s^{(n)} \cdot p_s^{(n)} \qquad \text{Solar Feed-in,} \tag{10}$$

$$in_{wl} = \sum_{n=1}^{N} w_{wl}^{(n)} \cdot p_{wl}^{(n)} \qquad \text{Onshore Feed-in,} \tag{11}$$

$$in_{wo} = \sum_{n=1}^{N} w_{wo}^{(n)} \cdot p_{wo}^{(n)} \qquad \text{Offshore Feed-in,} \tag{12}$$

where $w_s^{(n)}$, $w_{wl}^{(n)}$ and $w_{wo}^{(n)}$ denote the unknown weights (i.e., number of generators) of solar, onshore and offshore wind power generators at each transmission node $n = 1, \dots N$. Hence, the layout estimation aims to estimate the values of $w_s^{(n)}$, $w_{wl}^{(n)}$, and $w_{wo}^{(n)}$ such that the Mean Squared Error (MSE) is minimised for each generator type separately. From a technical perspective, this requires solving the popular *least squares* problem and corresponds to a linear regression setup. Such a setup is known to be unstable for highly correlated regressors, which leads to poorly determined estimated coefficients with high variance [70, cf. Section 3.4]. Since we expect weather data of neighbouring cells to be highly correlated, we also expect the given aggregated power signals $p_{(\cdot)}$ of each transmission node to be highly correlated with its neighbouring signals. Fig. 5 analyses the correlation of energy signals

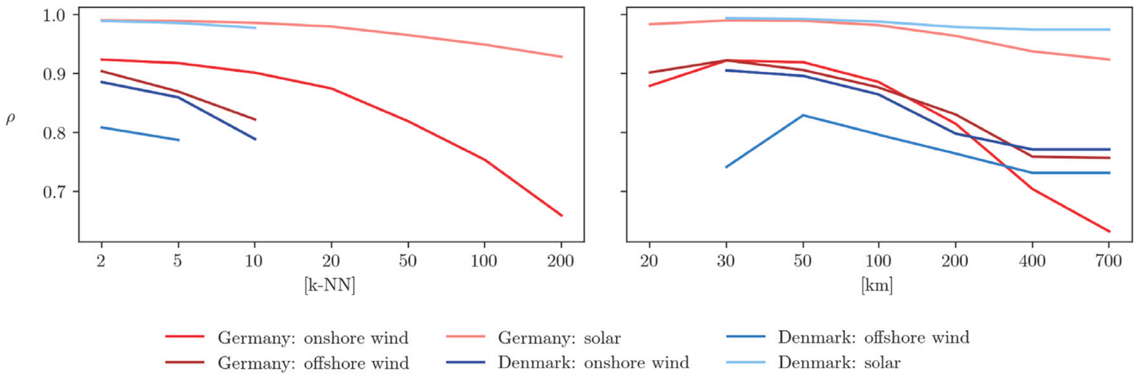

Fig. 5. Pearson correlation of power signals of 2019 from neighbouring transmission nodes for k-nearest neighbours (left) and given distance (right) per renewable generator type.

from neighbouring transmission nodes with respect to distance. The left plot visualises the mean correlation of every transmission node with its k-nearest-neighbours, while the right plot shows the mean correlation of all transmission nodes and all of their neighbours within the given distance in [km]. As expected, we observe strongly correlated signals, with the correlations only slightly decreasing in growing distances. Thus, the problem at hand shows high collinearities in the data and an alternative to using a simple linear regression is called for.

Therefore, the final estimation is done by using a regularised linear regression model for each generation type and country, i.e., an *elastic-net* with a L_1 and a L_2 regularisation term [see 71]. Within this framework, we optimise the strength of the regularisation via 10-fold cross-validation. Further, a non-negativity restriction for the coefficients is introduced to avoid unrealistic solutions, i.e., physically impossible solutions like a negative number of generators. The resulting optimisation problem is solved for each country and each year. Since the shrinkage of the estimated parameters is directly related to the variance of the features, i.e., the input signals, we standardise the features before optimising the parameters by

$$\tilde{p}_{s,t}^{(n)} = \frac{p_{s,t}^{(n)} - \overline{p}_{s}^{(n)}}{\sigma_{s}^{(n)}} \qquad \text{Solar,} \tag{13}$$

$$\tilde{p}_{wl,t}^{(n)} = \frac{p_{wl,t}^{(n)} - \overline{p}_{wl}^{(n)}}{\sigma_{wl}^{(n)}} \qquad \text{Onshore,} \tag{14}$$

$$\tilde{p}_{wo,t}^{(n)} = \frac{p_{wo,t}^{(n)} - \overline{p}_{wo}^{(n)}}{\sigma_{wo}^{(n)}} \qquad \text{Offshore,} \tag{15}$$

where $\tilde{p}_{\cdot,t}^{(n)}$ is the standardised power signal per generator type at time t and node n, $\overline{p}_{\cdot}^{(n)}$ the mean of all power signals at node n and $\sigma_{\cdot}^{(n)}$ the standard deviation of the power signals at node n. Note that doing so requires an intercept ($w_{\cdot}$) during estimation, which will result in nearly zero after reversing the standardisation. With this, the optimisation problem for the case of solar is given by

$$\underset{w_s}{\operatorname{argmin}} \left(in_s - \tilde{w}_s - \sum_{n=1}^{N} \tilde{w}_s^{(n)} \cdot \tilde{p}_s^{(n)} \right)^2 \tag{16}$$

$$+ \lambda \cdot \alpha \sum_{n=0}^{N} |\tilde{w}_s^{(n)}| + 0.5 \cdot \lambda \cdot (1-\alpha) \sum_{n=0}^{N} (\tilde{w}_s^{(n)})^2, \tag{17}$$

There, (16) minimises the difference between the true feed-in and our models' prediction, and (17) includes the regularisation terms.[4] The parameters $\tilde{w}_s^{(n)}$ denote the estimated weights in the standardised setup.

The standardisation is reversed after the optimisation to result in the installed capacities, i.e., by multiplying the calculated parameter values with the standard deviation of the corresponding original input data:

$$w_s^{(n)} = \tilde{w}_s^{(n)} \cdot \sigma_s^{(n)}. \tag{18}$$

The same optimisation is done for every year, both wind power generation types and each country separately.

Using an elastic-net regularisation is useful for two reasons. First, as we have seen in Fig. 5, aggregated power signals of the transmission nodes are highly correlated. We tackle this problem by using the L_2 regularisation term, which causes the regressors to act more like an orthogonal system, hence resulting in more stable estimations and a lower MSE [72]. Further, the L_2 penalty causes the resulting loss function to be strongly convex and avoids grouping effects of correlated variables [71]. The grouping effect means that within a heavily correlated group of regressors, it can be difficult to estimate the effects of each variable on the dependent variable accurately since another variable might partially or fully capture the effects of one variable. In our case, that would result in an estimation where all the weight is randomly assigned to a few transmission nodes. Besides the purely mathematical motivation of an easier and better estimation, the L_2 regularisation penalises very high negative and positive coefficients and thus avoids technically impossible solutions. Secondly, regularisation reduces the number of estimated weights to stabilise the estimation with limited data and results in a more realistic, compact model. A compact model improves the overall interpretability of results and reduces the noise in the estimated coefficients. Since the discussed L_2 penalty cannot set coefficients to zero, the L_1 regularisation here comes into play. It forces some of the estimated weights to zero, reducing the overall complexity. In summary, we use the L_2 ridge-like regularisation to shrink the coefficients of correlated predictors towards each other and the L_1 lasso-like regularisation to select variables, e.g., important generator locations, in the elastic-net approach.

The estimated weights represent the total installed generation units at the considered locations. By multiplying these with the nominal power of the used example generators, i.e., the nominal power of both wind turbines and the solar panel, we obtain the estimated capacities at each node. Altogether, the elastic-net results in completely data-driven layouts of renewable energy sources for each European country.

Remark 3.2. The estimation of installed capacities can also be done using standardised relative power signals. Relative power signals are derived by dividing the actual power signal of onshore, offshore and solar ($p_{wl}^{(n)}$, $p_{wo}^{(n)}$ and $p_{s}^{(n)}$) by the nominal power of the used power generator. These (standardised) relative power signals can now be used to replace the (standardised) actual power signals in the optimisation problem of the elastic-net (Formulas (16)–(17)). Thus, the estimated

---

[4] The hyperparameter α compromises between the L_1 and a L_2 regularisation term and is set to 0.7, as it has shown to be the best choice in our studies. The parameter λ is the cross-validated strength of regularisation.

and rescaled weights from the elastic-net directly correspond to the estimated installed capacity at each transmission node. Note that using relative or actual power signals results in the same estimated layout.

Estimated on such spatially and temporally high resolution, the working layouts mimic the wind, onshore and offshore, and solar power generation and realistically reflect the allocation of installed capacities over the landscape. However, *working layout* means here that the installed plants belonging to the estimated capacities are optimally utilised and *working* regarding used weather data set. They are always online and on the grid and are only limited by the level of wind and solar irradiation. Due to the objective of a purely data-driven approach, we do not make any assumptions about possible deviations of the potentially and optimally generated amount, e.g., due to self-consumption or storage in individual household batteries or the curtailment of PV and wind power plants, which is done to ensure grid stability. For example in Germany, PV power plants with a nominal power of up to 25 kW were only allowed to feed in a maximum of 70% of their nominal power until the beginning of 2023 due to concerns about grid congestion [73, §9(2)], and onshore wind energy is the most deregulated energy source, followed by offshore wind energy [74]. Due to the optimal utilisation of wind turbines and solar modules, we further do not consider wake effects of wind turbines standing next to each other in wind farms [31, e.g.,] and other possible reasons for losses, e.g., the age of the turbines and modules [29, e.g.,]. We, therefore, expect that the actual installed capacity is higher than technically necessary and that the estimated working layouts represent a lower bound compared to the actual total installed capacity.

Note that ignoring the high collinearity in our data and estimating the capacities by an ordinary least squares regression (OLS) also delivers suitable results, but only with respect to the production data. The layouts are able to mimic the actual power generation similarly well, but constitute highly unrealistic spatial allocations of the installed capacities. For example, onshore wind power generation in Germany is only allocated over 55 of 227 transmission nodes in 2022 (see Appendix A for more details).

It is also important to note that the correlation between wind locations in reanalysis data analogous to the correlation profile shown in Fig. 5 is typically higher than in measured data (see, e.g., [75]). As a result, the layouts derived to best model the aggregated feed-ins may exhibit slight deviations from those estimated using measured data instead of reanalysis data. For readers applying the code provided with this paper to different weather datasets, it is recommended that the resulting layouts be used primarily with the type of weather data from which they were originally estimated, to ensure consistency and accuracy in the results.

4. Results

In this section, we exemplary report the results for Germany and Denmark in detail. We analyse the ability of the estimated working layouts to mimic the actual feed-in of electricity per generator class (onshore wind, offshore wind, PV) and depict these layouts for solar and wind power generators across the countries for 2019 to 2022. We further demonstrate that the estimated layouts have been rather stable over the years and match the true installed capacities' allocation. Information on the estimations for all other countries of mainland Europe are provided in Appendix C.

First, we assess the ability of the estimated layouts to mimic the actual feed-in per generator type (onshore/offshore wind, PV). Fig. 6 depicts the actual and estimated PV generation for Germany (left) and Denmark (right) in July 2022. Besides minor deviations in the peak of each day, the estimation fits the actual generation and the changes between low and high-generation days are captured very well.

Similar observations can be made when considering the onshore wind generation in Fig. 7 and offshore wind generation in Fig. 8. Both types of wind generation are characterised by higher volatility, but the estimation generally fits the feed-in very well. Looking at the offshore wind feed-in in Denmark in detail, we notice a drop in wind generation on the 17th of July, 2022, which is not reflected in the estimate. This drop may be due to the curtailment of wind turbines and, thus, the limitation of wind energy. Since the approach presented here is based on converting weather data to feed-in data, it is not able to consider such curtailments.

Along with the visual evaluation, we assess the fit between synthetic and actual generation time series using quantitative measures. Our time series are compared with both actual feed-in data and alternative synthetic data from Renewables.ninja [47]. As the Renewables.ninja data is only available up to 2019, the comparison is limited to that year. For evaluating the quality and consistency of the time series, we employ both the root mean square error (RMSE) relative to the annual average generation of the same hour and additional metrics as suggested by [75] such as the Pearson correlation coefficient, the autocorrelation function (ACF), the difference of standard deviation of the first-difference time series relative to the standard deviation of the first-difference actual feed-in and a comparison of density functions. This approach allows us to compare not only point-wise generation levels but also the underlying structure of the time series, providing a comprehensive insight into the quality and characteristics of the synthetic time series. Thus, by utilising these error measures, deviations in the representation of the correlation between wind speeds or solar irradiation can be identified, helping to detect inaccuracies in the modelling process.

Table 3 reports the *Root Mean Squared Error* (RMSE) for the synthetic generation and, for the year 2019, for generation given by [47] relative to the respective realised hourly generation average and the Pearson correlation coefficient between synthetic generation data and actual generation. For the metrics in the case of solar, we only consider values of hours with an actual solar feed-in bigger than zero, thus excluding nighttime hours. A comparison of the synthetic feed-in data generated with the working layouts created in this work and [47] shows slightly higher RMSE of the data sets of [47], while the correlation through both synthetic generation time series is comparable high as shown in Table 3.

We also investigate the autocorrelation of the feed-in time series according to [75] to show how well the simulated data can represent the temporal variability of the measured data. Table 3 presents the differences between the autocorrelation function at lag one for the synthetic feed-in data and the actual feed-in data. Fig. 9 further illustrates the autocorrelation functions of the synthetic feed-in time series from the current working layouts, the synthetic data from Renewables.ninja, and the actual onshore wind feed-in for Germany and Denmark in 2019. Autocorrelation functions for the years 2020 to 2022 are provided in Appendix B. For 2019, the deviations in autocorrelations at lag one for both synthetic data sets are minimal, within the per mille range, with the exception of offshore wind in Denmark in the single-digit percentage range. The majority of deviations at lag one are slightly underestimated as [75] already observe for reanalysis wind data of the ERA5 data set, though not exclusively. The results in Fig. 9 confirm these small deviations in autocorrelations over all lags. While the autocorrelation function of synthetic feed-in based on [47] aligns more closely with the actual values for Denmark, the deviation for Germany in 2019 is noticeably larger than for the synthetic feed-in time series based on the layouts presented here.

Both the calculated lag-one values reported in Table 3 and the full autocorrelation functions, shown in Appendix B, demonstrate that synthetic data computed from the layouts adequately capture the structural patterns of the actual feed-in for all three generation types (onshore wind, offshore wind, and PV) across the period from 2019 to 2022. This confirms the robustness of the generated working layouts in reflecting actual feed-in behaviour.

In addition correctly reflecting the strong volatility of renewable energies is crucial. We use the standard deviation of the first-difference

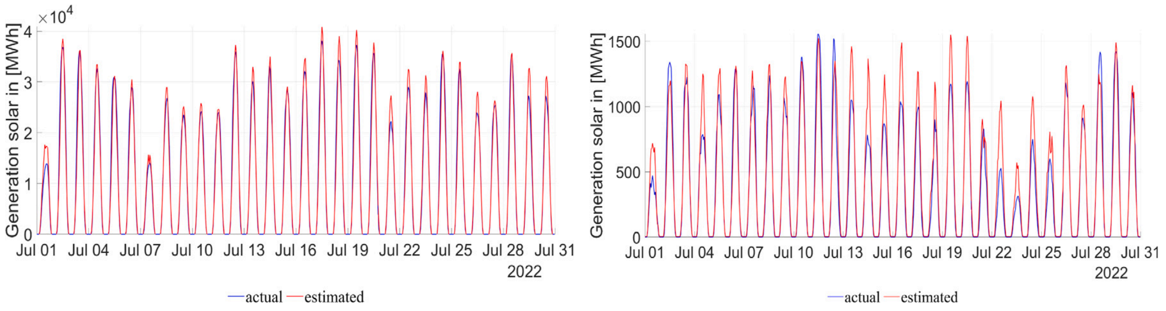

Fig. 6. Actual and estimated PV generation for Germany (left) and Denmark (right) in July 2022.

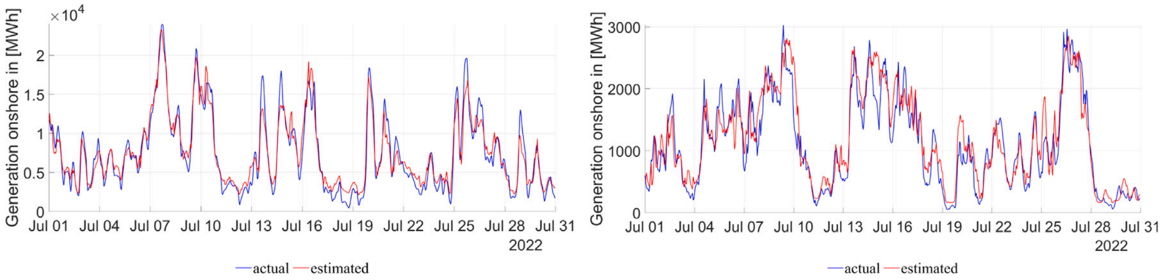

Fig. 7. Actual and estimated onshore wind generation for Germany (left) and Denmark (right) in July 2022.

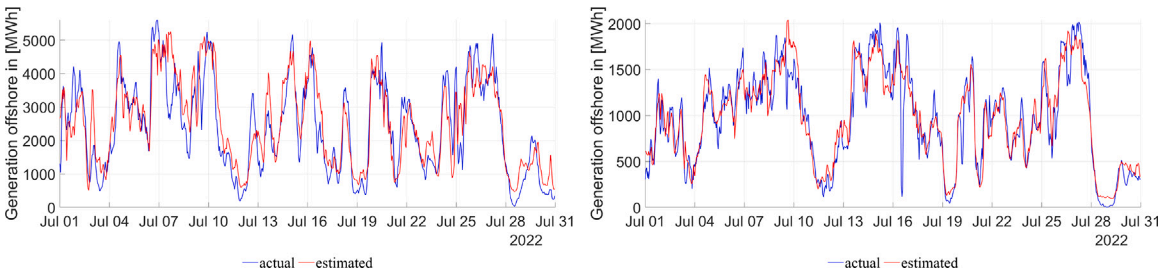

Fig. 8. Actual and estimated offshore wind generation for Germany (left) and Denmark (right) in July 2022.

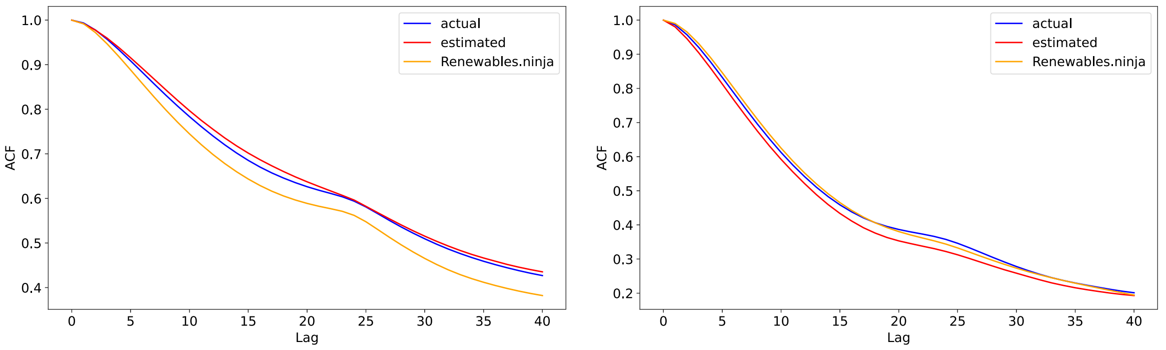

Fig. 9. Autocorrelation function for onshore wind generation for Germany (left) and Denmark (right) in 2019.

time series to describe the quality of the simulated data mapping the hourly ramps observable in the actual data, i.e. changes in the hourly feed-in values. In order to be able to compare the values across countries and generation datasets, Table 3 shows the difference between the standard deviations of the differentiated synthetic and real feed-in time series and divide these to the standard deviation of the differentiated real feed-in time series, i.e., the numbers represent percentage errors in the standard deviations of the differentiated synthetic time series.

Table 3

RMSE relative to the respective hourly generation average, Pearson correlation with actual data, difference of autocorrelation of synthetic and actual data relative to the autocorrelation of actual data and standard deviation of the first difference relative to the one from actual data; each of the elastic-net year- and country-wise estimation for PV, onshore wind and offshore wind generation and of renewable ninja data for PV, onshore wind and offshore wind generation for the year 2019 [47].

			2019 [47]	2019	2020	2021	2022
RMSE	PV	DEU	0.3356	0.2176	0.2028	0.2477	0.2040
		DNK	0.3380	0.2901	0.2631	0.3850	0.3597
	Onshore	DEU	0.2499	0.1358	0.1412	0.1462	0.1577
		DNK	0.2348	0.2966	0.3115	0.2997	0.2853
	Offshore	DEU	0.3950	0.2648	0.2653	0.3189	0.2861
		DNK	0.3515	0.3027	0.2505	0.2846	0.1986
Pearson	PV	DEU	0.9710	0.9735	0.9777	0.9671	0.9770
		DNK	0.9417	0.9549	0.9554	0.9615	0.9529
	Onshore	DEU	0.9580	0.9842	0.9837	0.9842	0.9820
		DNK	0.9528	0.9207	0.9090	0.9224	0.9270
	Offshore	DEU	0.8589	0.9037	0.9137	0.9015	0.9042
		DNK	0.8562	0.8852	0.9259	0.9135	0.9544
ACF	PV	DEU	−0.0061	−0.0023	−0.0022	−0.0042	−0.0016
		DNK	−0.0023	−0.0005	−0.0036	0.0016	0.0028
	Onshore	DEU	−0.0016	−0.0016	−0.0024	−0.0015	−0.0011
		DNK	0.0040	−0.0061	−0.0029	0.0021	−0.0025
	Offshore	DEU	0.0067	−0.0056	−0.0030	−0.0057	−0.0041
		DNK	0.0167	0.0118	0.0139	0.0090	0.0043
Diff. Standarddeviation	PV	DEU	0.1745	−0.0168	−0.0109	−0.0131	−0.0165
		DNK	0.0323	−0.0438	−0.0252	−0.0568	−0.0695
	Onshore	DEU	0.1892	0.1023	0.1547	0.0962	0.0419
		DNK	−0.1791	0.0998	−0.0131	−0.1493	0.0110
	Offshore	DEU	−0.2937	0.0428	−0.0250	0.0657	−0.0029
		DNK	−0.4383	−0.3645	−0.3812	−0.3385	−0.2145

The smaller the value, the better the data reflects the actual hourly changes in feed-in. The synthetic generation data based on [47] tend to overestimate ramp events in the PV and German onshore wind feed-in by double-digit percentages, while underestimating ramps in offshore wind and Danish onshore wind feed-in by similar margins. In contrast, the synthetic generation data based on the working layouts show larger underestimation only for offshore wind feed-in in Denmark. For German offshore wind feed-in, onshore wind and PV feed-in, deviations are generally within the single-digit percentage range. Overall, excepting Danish offshore wind feed-in, the layout-based synthetic feed-in closely simulate actual hourly feed-in variations with low discrepancies.

We complement the analysis by looking at the time series' distributions. Fig. 10 illustrates the distribution of solar feed-in values for 2019 in Germany and Denmark, presented as a histogram and a cumulative distribution function. Similar to the real data, both synthetic feed-in time series, generated by working layouts and based on [47], exhibit a concentration of values in lower generation range, effectively capturing the general distribution pattern. The generation spectrum is distributed analogue to the actual feed-in values with no systematic deviations, though individual fluctuations may differ in magnitude compared to the actual values. These discrepancies may be attributed to the use of reanalysis data and the exclusion of factors such as shutdowns, maintenance, and curtailments. A similar analysis is observed for onshore and offshore wind generation across the years 2019 to 2022, but with greater variability in the deviations, in particular at higher generation values and especially offshore.

In summary, in combination with the underlying weather data and the methodology used for weather-to-energy conversions, the generated working layouts accurately represent the real feed-in data in terms of absolute level, distribution and dependency structures at national aggregation and resolution. In a consecutive step, simple forecasts and nowcasts of the generated energy could be made with these estimated capacity layouts. However note, that proper forecasting is a much more complicated endeavour why we do not further elaborate on it in the following. For example, using capacity layouts based on historical data may result in forecasts that do not fully account for the upward trend in renewable energy deployment and therefore tend to have a downward bias. Higher forecast accuracy can be achieved by incorporating anticipated capacity increases at national level into the layout.

In the following, we directly analyse the estimated layouts and, thus, the estimated capacities. Table 4 compares the current total installed capacity of Denmark and Germany with the estimated total installed capacity for each year from 2019 to 2022. Thereby, the estimated total installed capacity is the sum of the estimated installed node capacities. The estimated total capacity of wind, onshore and offshore, and solar energy for Denmark and Germany deviates from the actual in all years. As expected, due to various factors limiting the measured feed-in, less capacity is required overall than is actually installed. We see that our approach requires about 44% less installed capacity for Germany and 13% less for Denmark to generate the given amount of photovoltaic feed-in. For wind, onshore and offshore, the deviation is smaller. In general, the deviation shows the high potential of renewable energy sources. Even without further expansion, optimal and unrestricted use of the installed plants would lead to increased power production from renewable energies.

Looking at the estimated working layouts more closely, we see that solar is mostly evenly distributed across Denmark (see Fig. 11). This aligns with our expectations since professional solar parks are emerging in every region, and PV panels are becoming more popular even for private households and investors. In Germany, we can also observe PV capacity distributed all over the land, but with a higher concentration in the south, especially in Bavaria (see Fig. 11). This reflects that Bavaria is the federal state with the most installed greenfield and rooftop PV capacity [78].

For the estimated German onshore wind capacities in Fig. 12, we observe more estimated capacities in the north than in the south of Germany. Interestingly, this reflects the allocation of wind turbines in Germany, where high wind-powered electricity generation in the north is often a problem for the nationwide grid infrastructure [74,78–81]. In Denmark, onshore wind capacity is not as evenly distributed as solar, with the highest installed capacity in the transmission node characterising the area of South Denmark (see Fig. 12). Compared to the other Danish transmission nodes, it captures the widest area and,

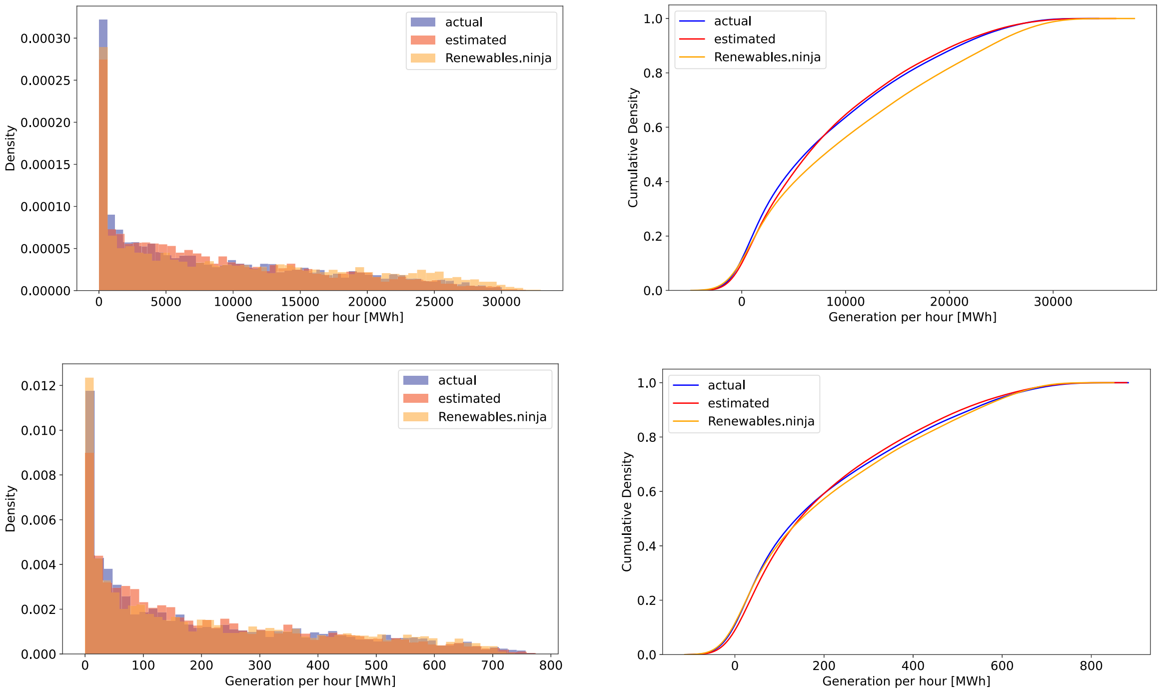

Fig. 10. Histogram (left) and cumulative distribution function (right) for solar generation for Germany (top) and Denmark (bottom) in 2019.

Table 4
Actual installed onshore wind, offshore wind and PV capacity [76,77] and estimated onshore wind, offshore wind and PV capacity of Denmark and Germany for each year in [MW].

Technology		PV		Onshore		Offshore	
Country		DNK	DEU	DNK	DEU	DNK	DEU
Actual installed	2019	1,014	45,299	4,426	52,792	1,700	6,393
	2020	1,013	48,206	4,402	53,184	1,700	7,504
	2021	1,300	53,302	4,481	54,499	1,700	7,774
	2022	1,536	57,744	4,644	55,289	2,305	7,787
Estimated installed	2019	641	24,842	3,327	47,064	1,316	5,084
	2020	804	27,248	3,069	48,530	1,400	5,567
	2021	930	28,622	2,802	51,010	1,804	5,672
	2022	1,341	32,285	3,218	51,354	2,042	5,232
Perc. deviation	2019	37%	45%	25%	11%	23%	20%
	2020	21%	43%	30%	9%	18%	26%
	2021	28%	46%	37%	6%	−6%	27%
	2022	13%	44%	31%	7%	11%	33%

thus, has a high potential for onshore wind power plants, represented by the layout's estimation. However, as with solar energy, Denmark's estimated onshore wind capacities are distributed throughout the country. This also corresponds to the allocation of installed wind turbines in Denmark [see 46].

Turning to Fig. 13, we see the estimated offshore wind capacity layout for Germany and Denmark. In Germany, most estimated high-capacity nodes are nearest nodes to the biggest offshore wind farms *GodeWind, Borkum Riffgrund* and *Hohe See* in the North Sea and *Baltic Eagle* in the Baltic Sea, as analysed in [44]. For Denmark, the transmission nodes have a larger catchment area than in Germany and, therefore, capture the installed capacity over a larger area, representing it on landscape nodes. This means that individual wind farms cannot be fully identified. Still, the two big wind farms *Horns Rev* in the North Sea and *Kriegers Flak* in the Baltic Sea as well as the haven *Esbjerg*, the central point for offshore wind energy in Denmark's North Sea, are represented in their corresponding nearest nodes with a high estimated installed capacity. Thus, we can conclude the layout identifying and mapping big wind farms.

Last, we investigate how stable the estimated capacity layouts are across the different years. We define stable estimates as those where capacities are allocated to the same transmission nodes each year. So a transmission node does not have any estimated capacity in one year, high estimated capacity the next year and none estimated capacity in the third year again. Therefore, we compare the estimated capacity per transmission node from 2019 to 2022 and analyse the development of offshore wind capacity as an example. Due to the small number of nodes in Germany (15 nodes) and Denmark (nine nodes), the results for this generation type can be presented clearly. For onshore wind and solar, the capacity developments at the individual nodes are more difficult to determine due to the high number of 227 transmission nodes for Germany. We present these results in Appendix B.

Fig. 14 plots the estimated capacity in [MW] per transmission node for offshore wind power generators for Germany and Denmark from 2019 to 2022. We can observe peaks to occur usually at the same transmission node. The estimated capacities do not fluctuate strongly over the years in both Germany and Denmark. In particular, no strong

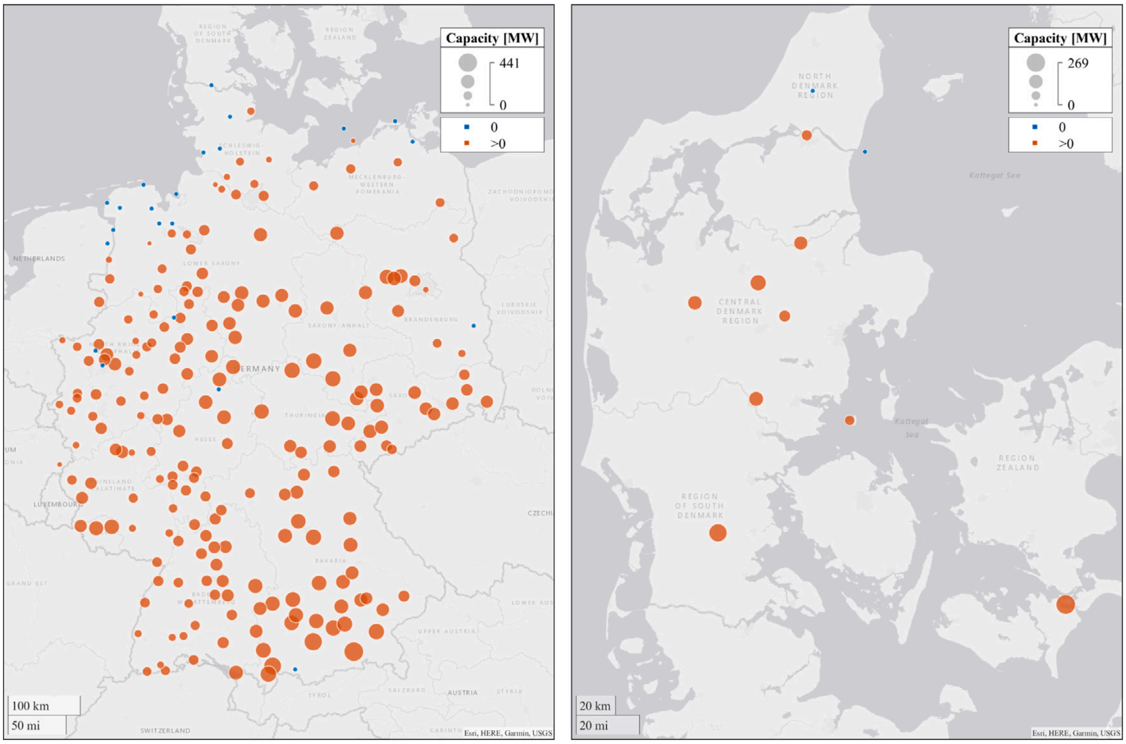

Fig. 11. Estimated PV capacity layout for Germany (left) and Denmark (right) in 2022.

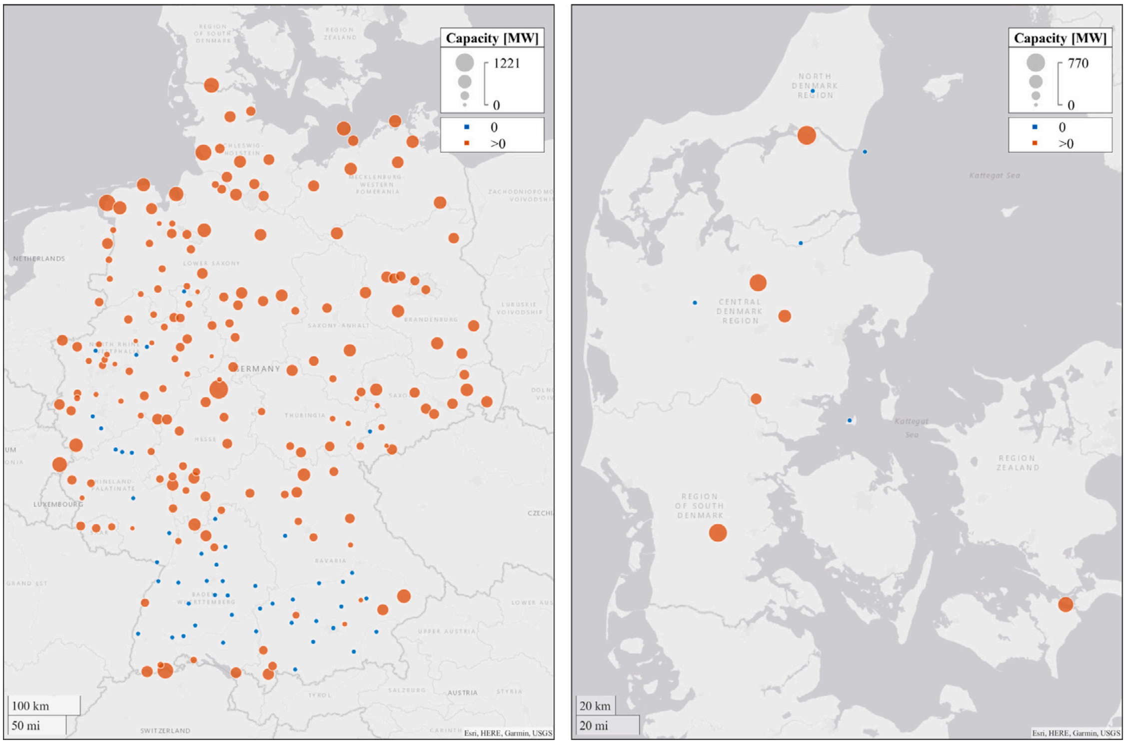

Fig. 12. Estimated onshore capacity layout for Germany (left) and Denmark (right) in 2022.

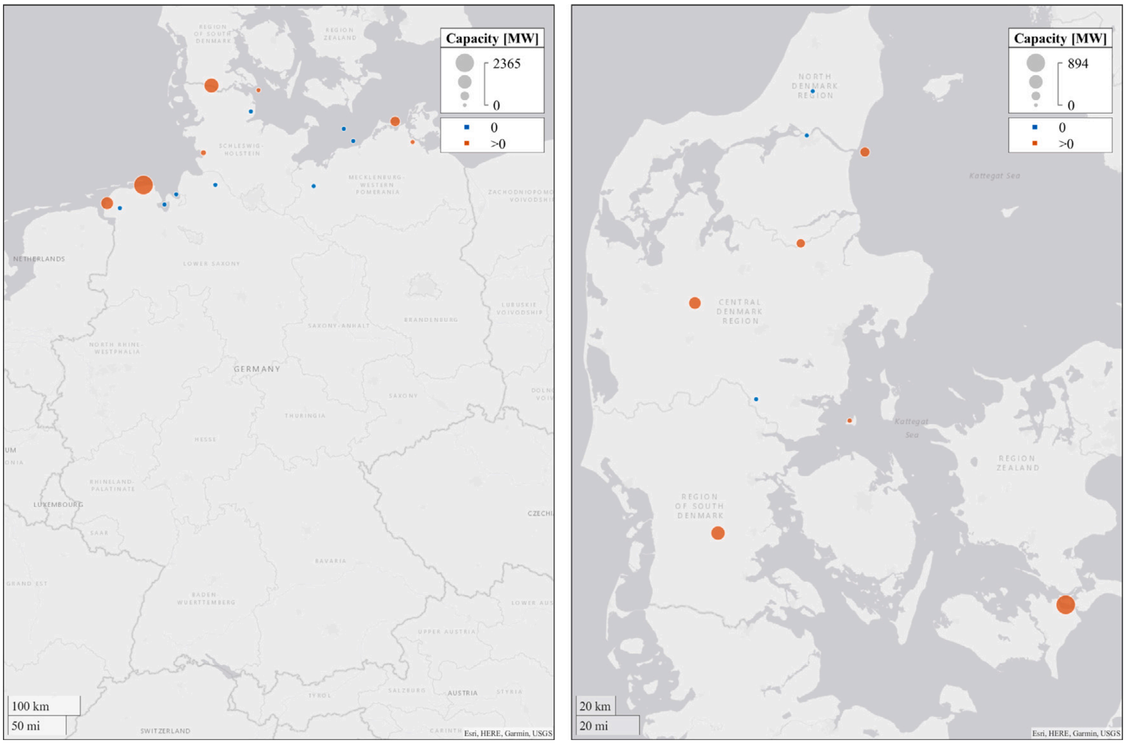

Fig. 13. Estimated offshore wind capacity layout for Germany (left) and Denmark (right) in 2022.

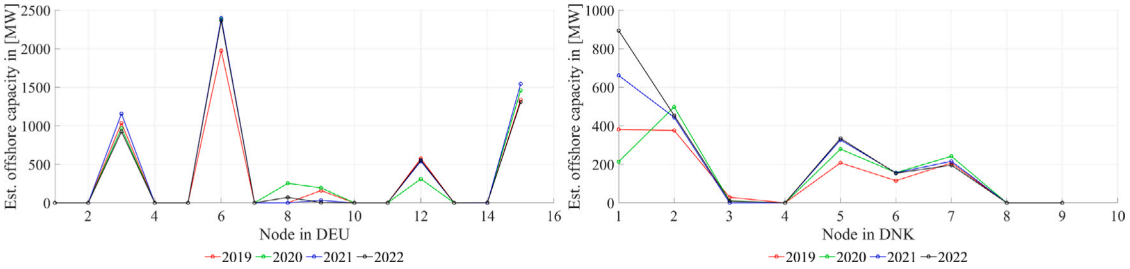

Fig. 14. Estimated node capacity for offshore wind for Germany (left) and Denmark (right) per year.

jumps from minimum to maximum values and back are observed. The almost constancy of the node capacities indicates a rather stable estimation over the years.

The contrary can be observed for results estimated by a non-regularised regression model. Due to a large number of transmission nodes and their highly correlated nature, estimated capacities cannot be estimated in a stable manner and a realistic allocation (see Appendix Fig. A.4). We prevent such behaviour using the proposed elastic-net regression, resulting in stable results for Denmark and Germany.

5. Summary and conclusion

In this paper, we describe a comprehensive methodology for developing synthetic, data-driven, and large-scale capacity layouts for onshore wind, offshore wind and solar power plants. The approach combines high-resolution numerical weather data with physical models of the power curves of wind turbines and solar modules to estimate potential installed wind and solar capacities at each network node of the main continental European transmission network. The methodology includes a country-specific regularised regression approach, combining synthetic outputs with actual measured wind and solar feed-in data to estimate the installed capacity at each node. The estimated layouts mimic the actual generated power by renewable generators very closely and thus are feasible as working layouts for further analysis.

We provide these realistic high-resolution layouts of installed onshore and offshore wind capacities as well as PV capacities in a comprehensive data set for mainland Europe, including generation data from 2019 to 2022 in an hourly resolution of all three types. By making the code publicly available, we enable others to generate results for a specific time horizon or location and tailor them to their needs. Layouts with any weather data, reanalysis data or real-time data, can be created and used. The paper provides a detailed understanding of the conversion process and the required variables to convert weather data to solar energy information.

Overall, the presented methodology and provided data sets offer valuable insights for policymakers and energy companies in designing and implementing renewable energy projects. The approach could be used to make forecasts in the resolution of single grid nodes with a given layout or to study the necessary or recommendable expansion of renewable generation capacities, also taking into account dark windless and sunny strong wind days to increase the share of renewable energies in the electricity mix. Additionally, through the data-driven calculation of layouts and feed-ins via weather-to-energy conversions, the effects of weather phenomena, e.g., storms or heat phases, on power generation from renewable energy sources can be analysed. In future research, the conversion process could be adapted and expanded. For instance, factors such as turbine wake effects, the unavailability of turbines and solar modules, and the efficiency degradation due to the ageing of turbines and modules could be considered. While this may not result in more accurate synthetic energy feed-ins compared to the working layouts presented here, it would generate layouts aimed at meeting the total actual installed capacity and not only to be proportionally to. Finally, the impact of adjusting solar feed-in data to account for stored solar energy and self-consumption can also be explored, considering the likely numerous regional and local differences, which would make this a highly complex and time-consuming undertaking.

CRediT authorship contribution statement

Oliver Grothe: Conceptualization, Data curation, Formal analysis, Funding acquisition, Investigation, Methodology, Resources, Supervision, Validation, Visualization, Writing – review & editing. **Fabian Kächele:** Conceptualization, Data curation, Formal analysis, Investigation, Methodology, Resources, Software, Validation, Visualization, Writing – original draft. **Mira Wälde:** Conceptualization, Data curation, Formal analysis, Investigation, Methodology, Resources, Software, Validation, Visualization, Writing – original draft.

Declaration of Generative AI and AI-assisted technologies in the writing process

During the preparation of this work the authors used ChatGPT by OpenAI (https://chat.openai.com.) in order to improve language and readability. After using this tool, the authors reviewed and edited the content as needed and take full responsibility for the content of the publication.

Declaration of competing interest

The authors declare the following financial interests/personal relationships which may be considered as potential competing interests: Mira Wälde reports financial support was provided by German Federal Ministry of Economic Affairs and Climate Action.

Acknowledge

The work was partly supported by the German Federal Ministry of Economic Affairs and Climate Action through the research project ProKoMo, Germany within the Systems Analysis Research Network of the 6th energy research program. Further, we thank Yanting Liu and Rafael Weinert for coding assistance. We also thank two anonymous referees for their insightful comments, which helped us to improve the paper.

Appendix A. Results for non-regularised capacity estimation

In this section, we report the results using a standard, non-regularised regression model for capacity estimation.

We observe that the total estimated installed capacity is comparable to the elastic-net estimation, but more nodes are set to an installed capacity of zero. Corresponding RMSE values, the total installed capacity per production type and the estimated generation for July 2022 for Germany and Denmark are shown in Table A.1 (RMSE), Table A.2 (capacity) and Figs. A.1 (PV), A.2 (onshore wind), A.3 (offshore wind).

Exemplary, Fig. A.4 shows the installed capacity for each German transmission node in 2019 and 2022, estimated by the non-regularised linear regression. We observe that, especially in the south, a large proportion of the nodes are assumed to have zero installed capacity, which does not correspond to a realistic capacity allocation. For example, wind turbines are installed in the Swabian Alb, located roughly in the middle-east of the federal state Baden-Wuerttemberg. [see, e.g., 82].

Consequently, the example of the onshore wind capacity allocation for Germany shows that the generated feed-in quantity relates to the installed capacity at a few grid nodes, which varies over the years. Thus, layouts generated with this estimation are not realistic and not stable. The estimated layouts can be used for feed-in forecasts of individual countries but do not provide any information on the allocation of installed capacities and generation.

Table A.1
RMSE of the ordinary-least-squares regression year- and country-wise estimation and prediction for PV, onshore wind and offshore wind generation relative to the respective hourly generation average.

			2019	2020	2021	2022
PV	DEU	est.	0.2146	0.1995	0.2437	0.1994
	DNK	est.	0.2897	0.2618	0.3834	0.3586
Onshore	DEU	est.	0.1329	0.1377	0.1430	0.1533
	DNK	est.	0.2959	0.3104	0.2986	0.2849
Offshore	DEU	est.	0.2638	0.2614	0.3168	0.2832
	DNK	est.	0.3026	0.2504	0.2845	0.1982

Table A.2
With an ordinary least-squares regression estimated onshore wind, offshore wind and PV capacity of Denmark and Germany for each year in [MW].

Technology	PV		Onshore		Offshore	
Country	DEU	DNK	DEU	DNK	DEU	DNK
2019	24,591	631	48,115	3,358	5,144	1,325
2020	26,988	800	48,742	3,113	5,634	1,407
2021	28,166	921	52,136	2,862	5,741	1,819
2022	31,987	1,326	51,094	3,255	5,294	2,058

Appendix B. Additional material for the layout evaluation

In this section, we provide further figures to evaluate the onshore wind and solar layout estimation for Germany and Denmark.

Figs. B.5 to B.8 show the autocorrelation function from 2019 to 2022 for synthetic PV generation and actual solar feed-in, synthetic offshore wind generation and actual offshore wind feed-in as well as synthetic onshore wind generation and actual onshore wind feed-in, in addition to Fig. 9 autocorrelation function of synthetic onshore wind generation and actual onshore wind feed-in for 2019.

Figs. B.9 to B.12 show the cumulative distribution function from 2019 to 2022 for synthetic onshore wind generation and actual onshore wind feed-in, synthetic offshore wind generation and actual offshore wind feed-in as well as synthetic PV generation and actual PV feed-in, in addition to Fig. 10.

Figs. B.13 and B.14 compare the estimated capacity per transmission node from 2019 to 2022 to account for stable layout estimations. The figures are in addition to Fig. 14 (estimated offshore wind power capacity per transmission node from 2019 to 2022) and show the estimated capacity in [MW] per transmission node for onshore wind and solar power generators from 2019 to 2022. As with offshore wind capacities, a stable level can be observed for onshore wind and solar capacities at the individual transmission nodes in Denmark. Here, the peaks usually occur at the same transmission nodes every year, too. We cannot observe details for the case of solar and onshore wind in Germany; however, the general level seems stable for most transmission nodes over the years.

Appendix C. European mainland capacity estimations

In this section, we report the estimated total installed capacity for each country, compared with the actual total installed capacity. Therefore, we first use data from the ENTSO-E transparency platform [53]. We fill in missing values with data provided by the online data query tool IRENASTAT [77], where the value of a year reflects the actual installed capacity at the end of the previous year. Values that have been supplemented accordingly are marked with a star (*) in the tables. Due to missing feed-in data provided by the ENTSO-E transparency platform [53], not all countries can be fully estimated. The results are reported in Tables C.3–C.5.

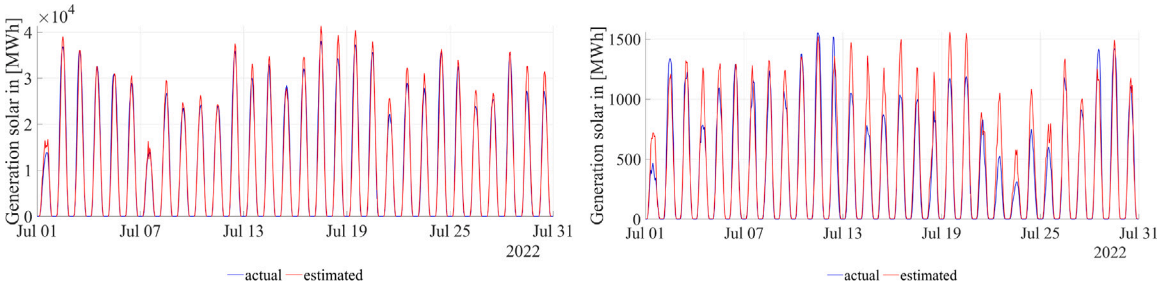

Fig. A.1. Actual and estimated PV generation for Germany (left) and Denmark (right) in July 2022 for the OLS regression.

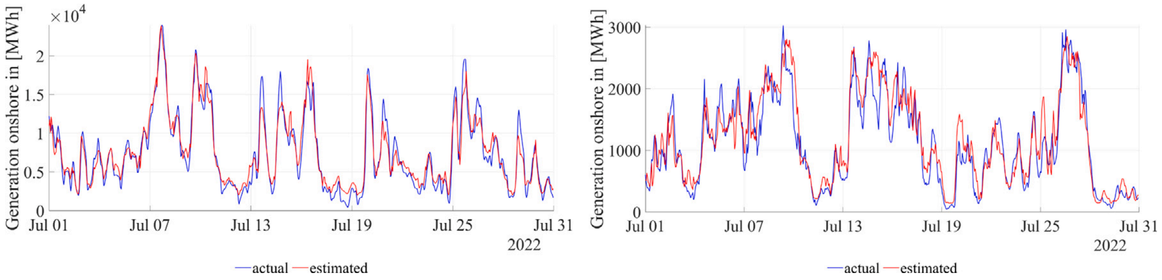

Fig. A.2. Actual and estimated onshore wind generation for Germany (left) and Denmark (right) in July 2022 for the OLS regression.

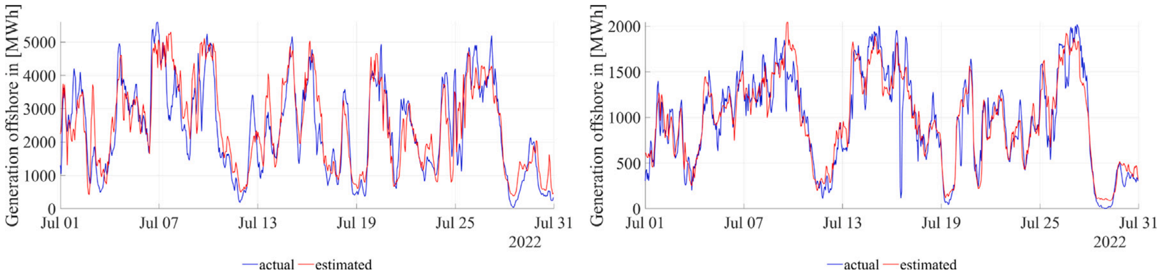

Fig. A.3. Actual and estimated offshore wind generation for Germany (left) and Denmark (right) in July 2022 for the OLS regression.

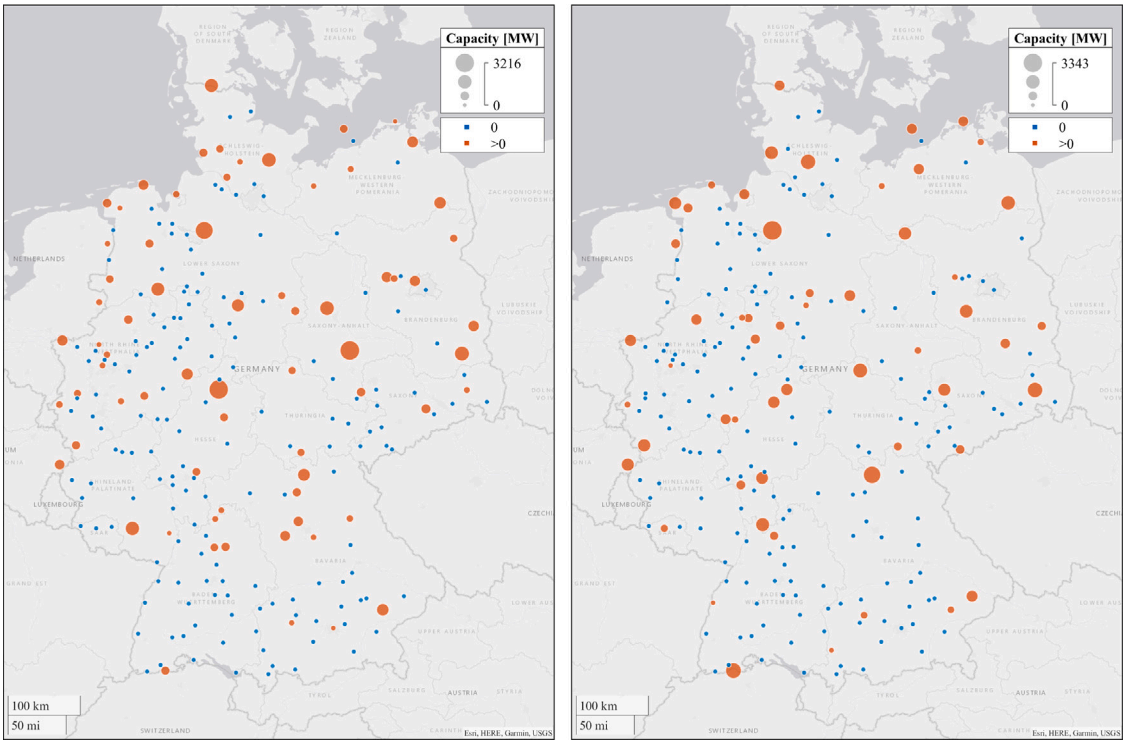

Fig. A.4. With an OLS regression estimated onshore wind capacity layout for Germany for 2019 (left) and 2022 (right).

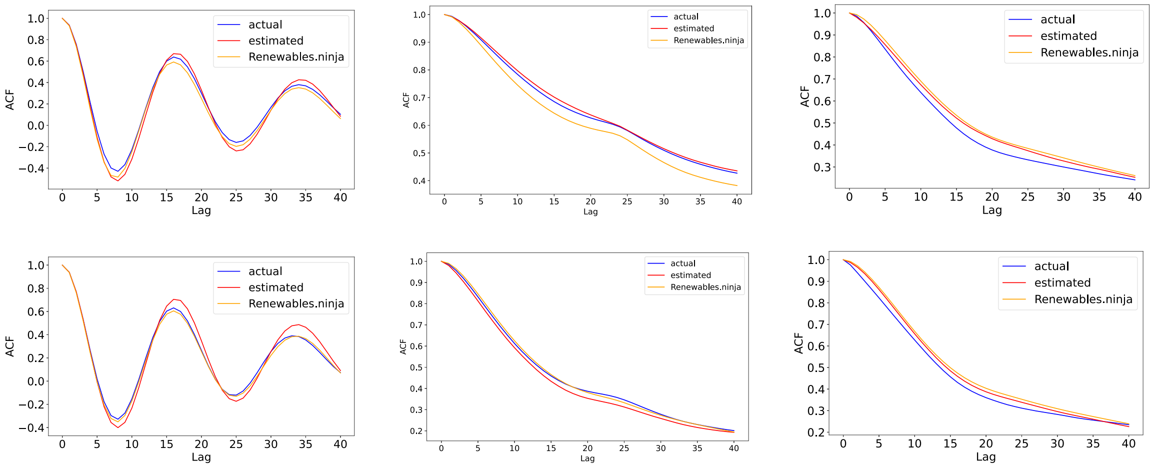

Fig. B.5. Autocorrelation function for solar (left), onshore wind (middle) and offshore wind (right) generation for Germany (top) and Denmark (bottom) in 2019.

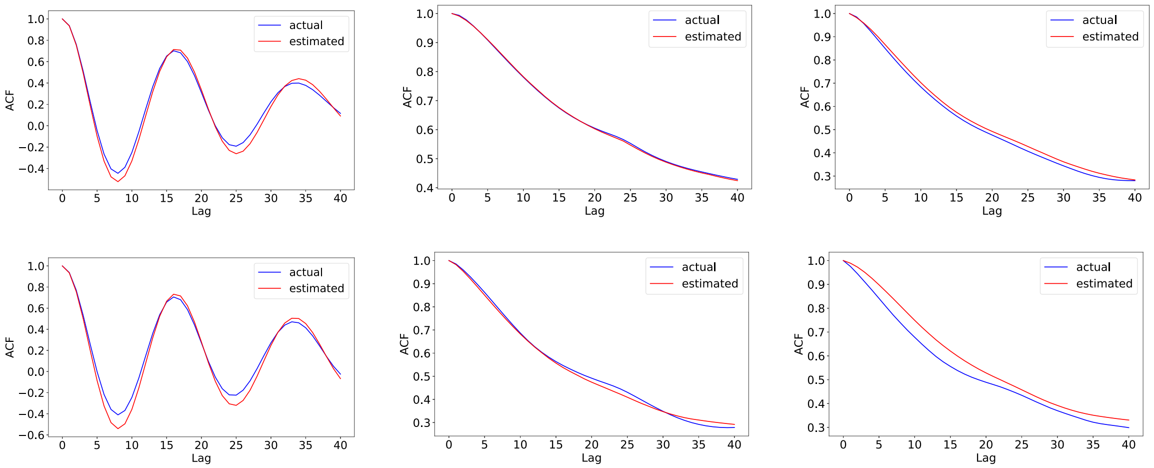

Fig. B.6. Autocorrelation function for solar (left), onshore wind (middle) and offshore wind (right) generation for Germany (top) and Denmark (bottom) in 2020.

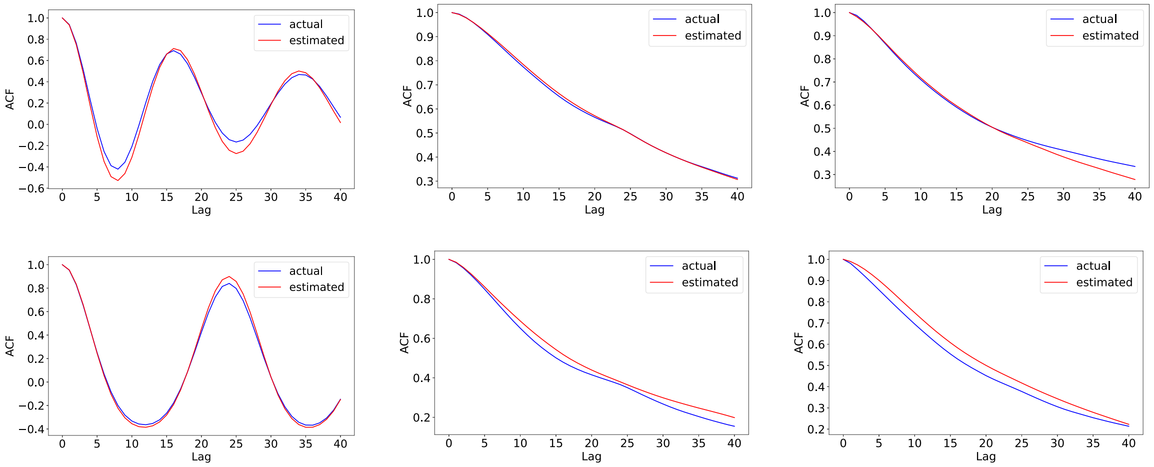

Fig. B.7. Autocorrelation function for solar (left), onshore wind (middle) and offshore wind (right) generation for Germany (top) and Denmark (bottom) in 2021.

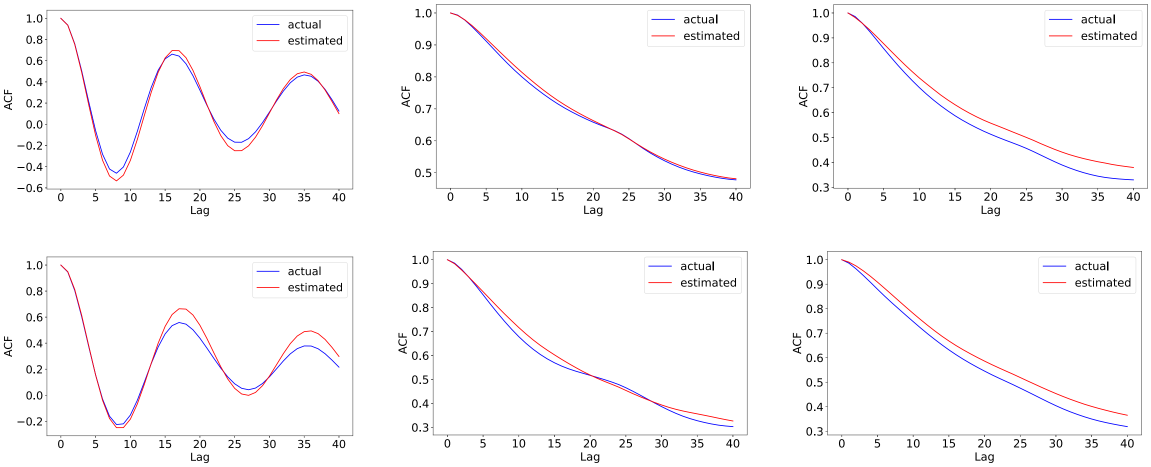

Fig. B.8. Autocorrelation function for solar (left), onshore wind (middle) and offshore wind (right) generation for Germany (top) and Denmark (bottom) in 2022.

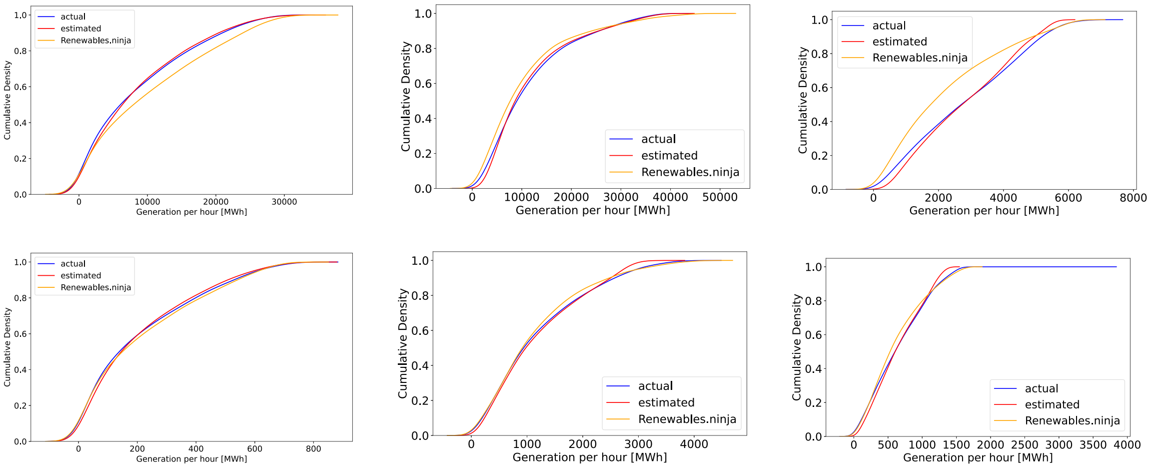

Fig. B.9. Cumulative distribution function for solar (left), onshore wind (middle) and offshore wind (right) generation for Germany (top) and Denmark (bottom) in 2019.

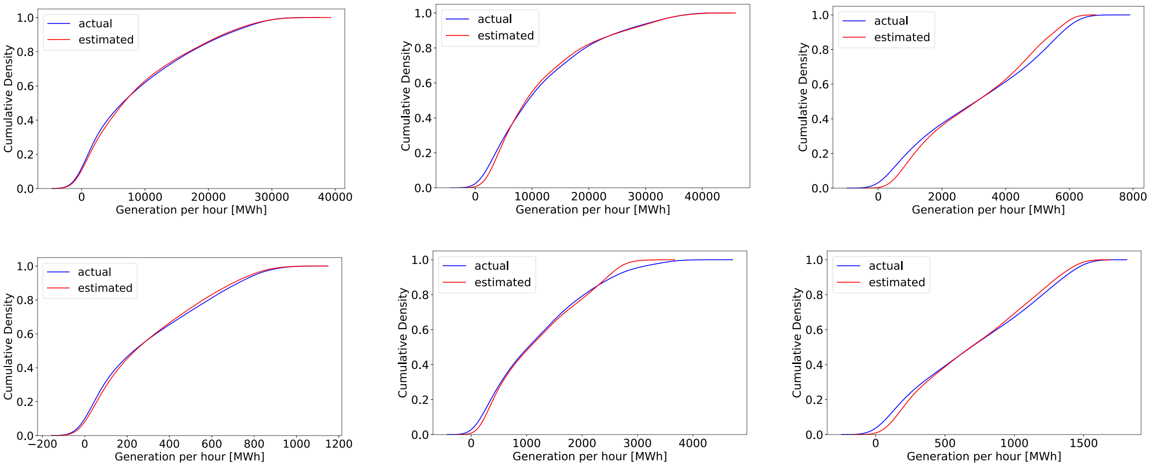

Fig. B.10. Cumulative distribution function for solar (left), onshore wind (middle) and offshore wind (right) generation for Germany (top) and Denmark (bottom) in 2020.

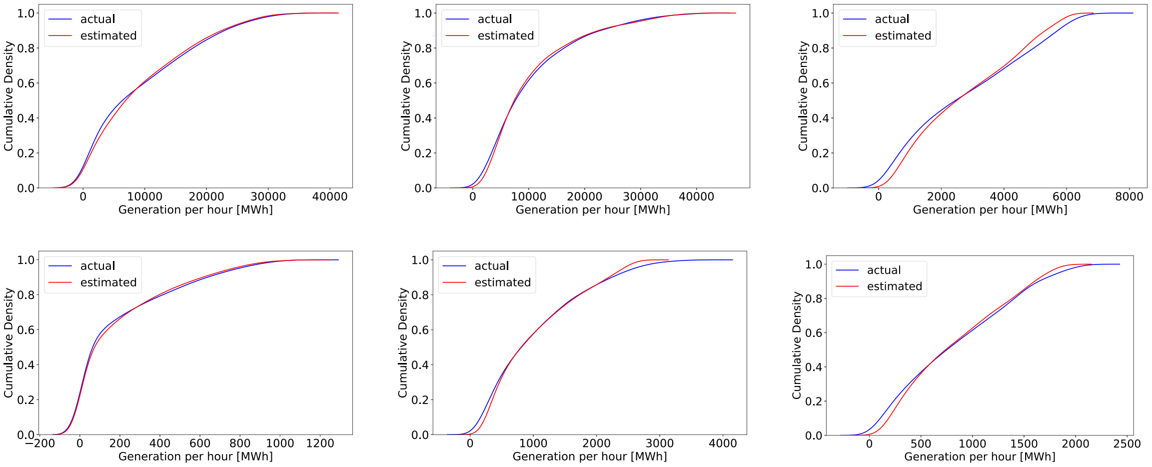

Fig. B.11. Cumulative distribution function for solar (left), onshore wind (middle) and offshore wind (right) generation for Germany (top) and Denmark (bottom) in 2021.

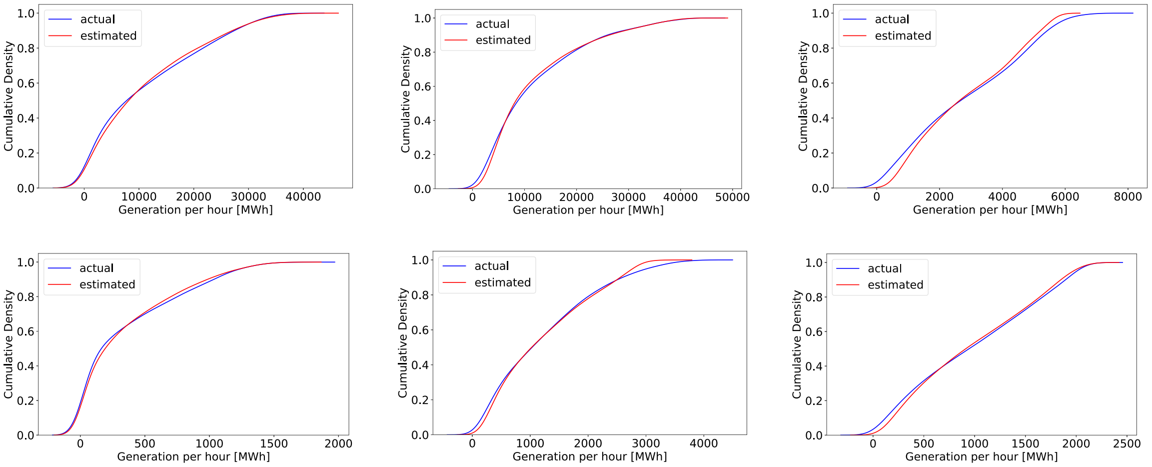

Fig. B.12. Cumulative distribution function for solar (left), onshore wind (middle) and offshore wind (right) generation for Germany (top) and Denmark (bottom) in 2022.

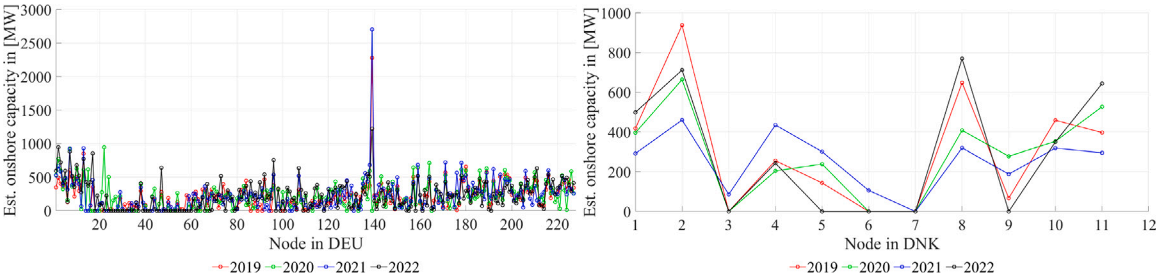

Fig. B.13. With the elastic-net regression estimated node capacity for onshore wind for Germany (left) and Denmark (right) per year.

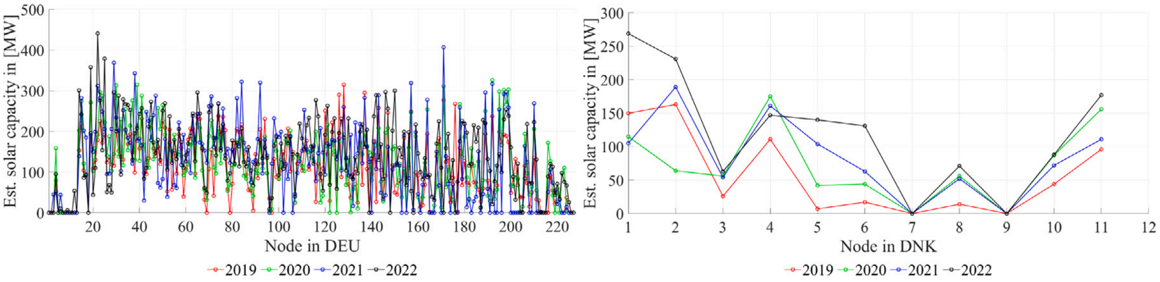

Fig. B.14. With the elastic-net regression estimated node capacity for solar for Germany (left) and Denmark (right) per year.

Table C.3
Actual installed onshore wind capacity [76,77] and estimated onshore wind capacity of all countries for each year in [MW].

Country	Actual				Estimated			
	2019	2020	2021	2022	2019	2020	2021	2022
Austria	3,035	3,133	3,198	3,500	3,406	4,093	4,570	4,160
Belgium	2,248	2,416	2,629	2,787	1,375	1,556	1,922	
Bulgaria	700	700	705	705	751	822	723	667
Bosnia Herzg	87	87	145	135	105	78	161	367
Switzerland	75*	75*	87*	87*	2,705	1,876	2,350	
Czechia	316	339	339	339	303	316	333	310
Germany	52,792	53,184	54,499	55,289	47,064	48,530	51,010	51,354
Denmark	4,426	4,402	4,481	4,644	3,327	3,069	2,802	3,218
Spain	22,961	24,447	26,664	27,735	22,961	24,332	31,046	
France	13,610	16,578	17,217	19,516	15,134	16,848		18,191
Greece	2,355	3,153	3,755	4,150	3,131	3,092	4,803	4,908
Croatia	616	739	796	925	668	859	1,021	1,304
Hungary	327	323	323	323		351	377	378
Italy	9,617	10,224	10,302	10,658	21,354	19,702	24,668	
Luxembourg	154	154	167	167	105	111	133	135
North Macedonia	35	37*	35	37		32	54	59
Montenegro	118	118	118	118	209	117	312	382
Netherlands	3,436	3,527	4,188	5,310	1,182	1,661	1,769	1,939
Poland	5,808	5,953	6,570	7,950	5,779	6,149	6,935	7,887
Portugal	5,127	5,181	5,183	5,328	6,138	6,425	6,539	6,900
Romania	2,968	2,972	2,957	2,957		3,774		
Serbia	398	397	429	533				664
Slovakia	3	3	3	4*			2	2
Slovenia	3	3	3	2		1	2	2

Table C.4
Actual installed offshore wind capacity [76,77] and estimated offshore wind capacity of all countries for each year in [MW].

Country	Actual				Estimated			
	2019	2020	2021	2022	2019	2020	2021	2022
Belgium	1,548	2,254	2,254	2,254				
Germany	6,393	7,504	7,774	7,787	5,084	5,567	5,672	5,232
Denmark	1,700	1,700	1,700	2,305	1,316	1,400	1,804	2,042
France	2*	14	10	20				
Netherlands	957	957	2,460	2,460	833	1,243	2,214	2,165
Portugal	0	8*	25	25	0	13	14	29

Table C.5
Actual installed PV capacity [76,77] and estimated PV capacity of all countries for each year in [MW].

Country	Actual				Estimated			
	2019	2020	2021	2022	2019	2020	2021	2022
Austria	1,193	1,333	1,851	2,500	356	440	453	403
Belgium	3,369	3,887	4,788	4,788	2,084	2,541	2,908	
Bulgaria	1,059	1,084	1,246	1,726	637	675	740	856
Switzerland	2,173*	2,498*	2,973*	3,449*		1,084	1,056	
Czechia	2,049	2,061	2,054	2,053		1,298	1,286	1,389
Germany	45,299	48,206	53,302	57,744	24,842	27,248	28,622	32,285
Denmark	1,014	1,013	1,300	1,536	641	804	930	1,341
Spain	6,751	8,466	11,390	14,640	4,617	6,439	8,761	
France	8,188	9,438	10,213	13,154	6,264	6,673	7,470	8,347
Greece	2,441	2,606	3,055	3,820	1,756	1,946	2,147	2,598
Croatia	53	53	85	96	35	38	42	47
Hungary	936	1,407	1,829	2,524	766	856	1,254	1,567
Italy	4,717	4,874	4,979	5,137	8,767	9,143	9,177	
Luxembourg	136	170	236	258	73	87	115	146
North Macedonia	21*	26*	94*	94*				
Netherlands[a]	4,608	7,226	11,108	14,911	39	129	201	219
Poland	430	1,310	3,473	6,664		979	2,770	5,402
Portugal	324	413	569	1,032	397	480	650	970
Romania	1,150	1,163	1,145	1,160	616	693	696	845
Serbia	21*	23*	31*	52*				
Slovakia	531	531	532	536*	278	318	283	295
Slovenia	275	278	289	286	130	129	141	141

[a] Solar generation data provided by [53] is incomplete for all years and thus, the estimated capacities are far too low.

Data availability

The data and the code to produce the data presented in this study are openly available. The code is provided in a GitHub repository through the following link: https://github.com/MWaterm/High-Resolution-Working-Layouts-and-Time-Series-for-Renewable-Energy-Generation-in-Europe. The data set can be downloaded through the following link: https://doi.org/10.6084/m9.figshare.22439254. The data are generated using Copernicus Climate Change Service information [2019-2022], containing modified Copernicus Climate Change Service information [2019-2022].

References

[1] European Commission EU, Communication from the commission to The European parliament, The Council, The European economic and Social Committee and the Committee of the Regions the European green deal, 2019, https://eur-lex.europa.eu/legal-content/EN/TXT/?qid=1576150542719&uri=COM%3A2019%3A640%3AFIN, (Accessed 15 November 2022).

[2] European Commission, Directorate-General for Climate Action, Directorate-General for Energy, Directorate-General for Mobility and Transport, A. De Vita, P. Capros, L. Paroussos, K. Fragkiadakis, P. Karkatsoulis, L. Höglund-Isaksson, W. Winiwarter, P. Purohit, A. Gómez-Sanabria, P. Rafaj, L. Warnecke, A. Deppermann, M. Gusti, S. Frank, P. Lauri, F. Fulvio, A. Florou, M. Kannavou, N. Forsell, T. Fotiou, P. Siskos, P. Havlík, I. Tsiropoulos, S. Evangelopoulou, P. Witzke, M. Kesting, N. Katoufa, I. Mitsios, G. Asimakopoulou, T. Kalokyris, EU reference scenario 2020: energy, transport and GHG emissions: trends to 2050, 2021, http://dx.doi.org/10.2833/35750, Publications Office.

[3] Juan M. Morales, Antonio J. Conejo, Henrik Madsen, Pierre Pinson, Marco Zugno, Integrating Renewables in Electricity Markets, in: International Series in Operations Research & Management Science. 205SpringerLinkSpringer eBook Collection, Springer, Boston, MA, ISBN: 978-1-4614-9410-2, 2014, http://dx.doi.org/10.1007/978-1-4614-9411-9.

[4] Hugo A. Gil, Catalina Gomez-Quiles, Jesus Riquelme, Large-scale wind power integration and wholesale electricity trading benefits: Estimation via an ex post approach, Energy Policy (ISSN: 0301-4215) 41 (2012) 849–859, http://dx.doi.org/10.1016/j.enpol.2011.11.067, Modeling Transport (Energy) Demand and Policies.

[5] Werner Antweiler, Felix Muesgens, On the long-term merit order effect of renewable energies, Energy Econ. (ISSN: 0140-9883) 99 (2021) 105275, http://dx.doi.org/10.1016/j.eneco.2021.105275.

[6] Philip Beran, Christian Pape, Christoph Weber, Modelling german electricity wholesale spot prices with a parsimonious fundamental model – validation & application, Util. Policy (ISSN: 0957-1787) 58 (2019) 27–39, http://dx.doi.org/10.1016/j.jup.2019.01.008, URL https://www.sciencedirect.com/science/article/pii/S0957178719300359.

[7] Christian Pape, Simon Hagemann, Christoph Weber, Are fundamentals enough? Explaining price variations in the German day-ahead and intraday power market, Energy Econ. (ISSN: 0140-9883) 54 (2016) 376–387, http://dx.doi.org/10.1016/J.ENECO.2015.12.013.

[8] I. González-Aparicio, F. Monforti, P. Volker, A. Zucker, F. Careri, T. Huld, J. Badger, Simulating European wind power generation applying statistical downscaling to reanalysis data, Appl. Energy (ISSN: 0306-2619) 199 (2017) 155–168, http://dx.doi.org/10.1016/j.apenergy.2017.04.066.

[9] Huaizhi Wang, Zhenxing Lei, Xian Zhang, Bin Zhou, Jianchun Peng, A review of deep learning for renewable energy forecasting, Energy Convers. Manage. (ISSN: 0196-8904) 198 (2019) 111799, http://dx.doi.org/10.1016/j.enconman.2019.111799.

[10] Gangqiang Li, Sen Xie, Bozhong Wang, Jiantao Xin, Yunfeng Li, Shengnan Du, Photovoltaic power forecasting with a hybrid deep learning approach, IEEE Access 8 (2020) 175871–175880, http://dx.doi.org/10.1109/ACCESS.2020.3025860.

[11] Farah Shahid, Aneela Zameer, Mudasser Afzal, Muhammad Hassan, Short term solar energy prediction by machine learning algorithms, 2020, http://dx.doi.org/10.48550/ARXIV.2012.00688, arXiv.

[12] Katarzyna Maciejowska, Weronika Nitka, Tomasz Weron, Enhancing load, wind and solar generation for day-ahead forecasting of electricity prices, Energy Econ. (ISSN: 01409883) 99 (2021) 105273, http://dx.doi.org/10.1016/j.eneco.2021.105273.

[13] Zunaib Ali, Ghanim Putrus, Mousa Marzband, Mahsa Bagheri Tookanlou, Komal Saleem, Pravat Kumar Ray, Bidyadhar Subudhi, Online sensorless solar power forecasting for microgrid control and automation, in: 2021 International Symposium of Asian Control Association on Intelligent Robotics and Industrial Automation, IRIA, 2021, pp. 443–448, http://dx.doi.org/10.1109/IRIA53009.2021.9588690.

[14] Ningkai Tang, Shiwen Mao, Yu Wang, R.M. Nelms, Solar power generation forecasting with a lasso-based approach, IEEE Internet Things J. 5 (2) (2018) 1090–1099, http://dx.doi.org/10.1109/JIOT.2018.2812155.

[15] Yuhao Nie, Quentin Paletta, Andea Scott, Luis Martin Pomares, Guillaume Arbod, Sgouris Sgouridis, Joan Lasenby, Adam Brandt, Sky image-based solar forecasting using deep learning with heterogeneous multi-location data: Dataset fusion versus transfer learning, Appl. Energy (ISSN: 0306-2619) 369 (2024) 123467, http://dx.doi.org/10.1016/j.apenergy.2024.123467, URL https://www.sciencedirect.com/science/article/pii/S030626192400850X.

[16] Hugo T.C. Pedro, Carlos F.M. Coimbra, Assessment of forecasting techniques for solar power production with no exogenous inputs, Sol. Energy (ISSN: 0038-092X) 86 (7) (2012) 2017–2028, http://dx.doi.org/10.1016/j.solener.2012.04.004, URL https://www.sciencedirect.com/science/article/pii/S0038092X12001429.

[17] R. Tawn, J. Browell, A review of very short-term wind and solar power forecasting, Renew. Sustain. Energy Rev. (ISSN: 1364-0321) 153 (2022) 111758, http://dx.doi.org/10.1016/j.rser.2021.111758.

[18] Shyam Singh Chandel, Ankit Gupta, Rahul Chandel, Salwan Tajjour, Review of deep learning techniques for power generation prediction of industrial solar photovoltaic plants, Solar Compass (ISSN: 2772-9400) 8 (2023) 100061, http://dx.doi.org/10.1016/j.solcom.2023.100061, URL https://www.sciencedirect.com/science/article/pii/S2772940023000292.

[19] Wassila Tercha, Sid Ahmed Tadjer, Fathia Chekired, Laurent Canale, Machine learning-based forecasting of temperature and solar irradiance for photovoltaic systems, Energies (ISSN: 1996-1073) 17 (5) (2024) http://dx.doi.org/10.3390/en17051124, URL https://www.mdpi.com/1996-1073/17/5/1124.

[20] Rial A. Rajagukguk, Raden A.A. Ramadhan, Hyun-Jin Lee, A review on deep learning models for forecasting time series data of solar irradiance and photovoltaic power, Energies (ISSN: 1996-1073) 13 (24) (2020) http://dx.doi.org/10.3390/en13246623.

[21] Marco Pierro, Damiano Gentili, Fabio Romano Liolli, Cristina Cornaro, David Moser, Alessandro Betti, Michela Moschella, Elena Collino, Dario Ronzio, Dennis van der Meer, Progress in regional pv power forecasting: A sensitivity analysis on the italian case study, Renew. Energy (ISSN: 0960-1481) 189 (2022) 983–996, http://dx.doi.org/10.1016/j.renene.2022.03.041, URL https://www.sciencedirect.com/science/article/pii/S0960148122003184.

[22] Cyril Voyant, Gilles Notton, Soteris Kalogirou, Marie-Laure Nivet, Christophe Paoli, Fabrice Motte, Alexis Fouilloy, Machine learning methods for solar radiation forecasting: A review, Renew. Energy (ISSN: 0960-1481) 105 (2017) 569–582, http://dx.doi.org/10.1016/j.renene.2016.12.095, URL https://www.sciencedirect.com/science/article/pii/S0960148116311648.

[23] R. Ahmed, V. Sreeram, Y. Mishra, M.D. Arif, A review and evaluation of the state-of-the-art in PV solar power forecasting: Techniques and optimization, Renew. Sustain. Energy Rev. (ISSN: 1364-0321) 124 (2020) 109792, http://dx.doi.org/10.1016/j.rser.2020.109792.

[24] Adel Mellit, Soteris A. Kalogirou, Artificial intelligence techniques for photovoltaic applications: A review, Prog. Energy Combust. Sci. (ISSN: 0360-1285) 34 (5) (2008) 574–632, http://dx.doi.org/10.1016/j.pecs.2008.01.001, URL https://www.sciencedirect.com/science/article/pii/S0360128508000026.

[25] Xiaochen Wang, Peng Guo, Xiaobin Huang, A Review of Wind Power Forecasting Models, Energy Procedia (ISSN: 1876-6102) 12 (2011) 770–778, http://dx.doi.org/10.1016/j.egypro.2011.10.103, The Proceedings of International Conference on Smart Grid and Clean Energy Technologies (ICSGCE 2011).

[26] Ezgi Arslan Tuncar, Şafak Sağlam, Bülent Oral, A review of short-term wind power generation forecasting methods in recent technological trends, Energy Rep. (ISSN: 2352-4847) 12 (2024) 197–209, http://dx.doi.org/10.1016/j.egyr.2024.06.006, URL https://www.sciencedirect.com/science/article/pii/S2352484724003603.

[27] Matti Koivisto, Guðrún Margrét Jónsdóttir, Poul Sørensen, Konstantinos Plakas, Nicolaos Cutululis, Combination of meteorological reanalysis data and stochastic simulation for modelling wind generation variability, Renew. Energy (ISSN: 0960-1481) 159 (2020) 991–999, http://dx.doi.org/10.1016/j.renene.2020.06.033.

[28] Iain Staffell, Stefan Pfenninger, Using bias-corrected reanalysis to simulate current and future wind power output, Energy (ISSN: 0360-5442) 114 (2016) 1224–1239, http://dx.doi.org/10.1016/j.energy.2016.08.068.

[29] Iain Staffell, Richard Green, How does wind farm performance decline with age? Renew. Energy (ISSN: 0960-1481) 66 (2014) 775–786, http://dx.doi.org/10.1016/j.renene.2013.10.041.

[30] M.L. Kubik, D.J. Brayshaw, P.J. Coker, J.F. Barlow, Exploring the role of reanalysis data in simulating regional wind generation variability over Northern Ireland, Renew. Energy (ISSN: 0960-1481) 57 (2013) 558–561, http://dx.doi.org/10.1016/j.renene.2013.02.012.

[31] R.J. Barthelmie, S.C. Pryor, S.T. Frandsen, K.S. Hansen, J.G. Schepers, K. Rados, W. Schlez, A. Neubert, L.E. Jensen, S. Neckelmann, Quantifying the impact of wind turbine wakes on power output at offshore wind farms, J. Atmos. Ocean. Technol. 27 (8) (2010) 1302–1317, http://dx.doi.org/10.1175/2010JTECHA1398.1.

[32] R.W. Baker, S.N. Walker, J.E. Wade, Annual and seasonal variations in mean wind speed and wind turbine energy production, Sol. Energy (ISSN: 0038-092X) 45 (5) (1990) 285–289, http://dx.doi.org/10.1016/0038-092X(90)90013-3.

[33] Stephen Rose, Jay Apt, What can reanalysis data tell us about wind power? Renew. Energy (ISSN: 0960-1481) 83 (2015) 963–969, http://dx.doi.org/10.1016/j.renene.2015.05.027.

[34] Gordon Hughes, The performance of wind farms in the United Kingdom and Denmark, 2012, URL https://www.ref.org.uk/attachments/article/280/ref.hughes.19.12.12.pdf. (Accessed 03 March 2023).

[35] Keith M. Sunderland, Mahinsasa Narayana, Ghanim Putrus, Michael F. Conlon, Steve McDonald, The cost of energy associated with micro wind generation: International case studies of rural and urban installations, Energy (ISSN: 0360-5442) 109 (2016) 818–829, http://dx.doi.org/10.1016/j.energy.2016.05.045.

[36] Darragh Kenny, Stephanie Fiedler, Which gridded irradiance data is best for modelling photovoltaic power production in Germany? Sol. Energy (ISSN: 0038-092X) 232 (2022) 444–458, http://dx.doi.org/10.1016/j.solener.2021.12.044.

[37] Christopher Frank, Stephanie Fiedler, Susanne Crewell, Balancing potential of natural variability and extremes in photovoltaic and wind energy production for European countries, Renew. Energy (ISSN: 0960-1481) 163 (2021) 674–684, http://dx.doi.org/10.1016/j.renene.2020.07.103.

[38] Thomas Huld, Gabi Friesen, Artur Skoczek, Robert P. Kenny, Tony Sample, Michael Field, Ewan D. Dunlop, A power-rating model for crystalline silicon PV modules, Sol. Energy Mater. Sol. Cells (ISSN: 0927-0248) 95 (12) (2011) 3359–3369, http://dx.doi.org/10.1016/j.solmat.2011.07.026.

[39] Thomas Huld, Ana M. Gracia Amillo, Estimating PV module performance over Large Geographical Regions: The role of irradiance, air temperature, wind speed and solar spectrum, Energies (ISSN: 1996-1073) 8 (6) (2015) 5159–5181, http://dx.doi.org/10.3390/en8065159.

[40] Stefan Pfenninger, Iain Staffell, Long-term patterns of European PV output using 30 years of validated hourly reanalysis and satellite data, Energy (ISSN: 0360-5442) 114 (2016) 1251–1265, http://dx.doi.org/10.1016/j.energy.2016.08.060.

[41] Adam Piasecki, Jakub Jurasz, Alexander Kies, Measurements and reanalysis data on wind speed and solar irradiation from energy generation perspectives at several locations in Poland, SN Appl. Sci. 1 (8) 2019, http://dx.doi.org/10.1007/s42452-019-0897-2.

[42] Thorsten Engelhorn, Felix Müsgens, How to estimate wind-turbine infeed with incomplete stock data: A general framework with an application to turbine-specific market values in Germany, Energy Econ. (ISSN: 0140-9883) 72 (2018) 542–557, http://dx.doi.org/10.1016/j.eneco.2018.04.022.

[43] Jon Olauson, Mikael Bergkvist, Modelling the Swedish wind power production using MERRA reanalysis data, Renew. Energy (ISSN: 0960-1481) 76 (2015) 717–725, http://dx.doi.org/10.1016/j.renene.2014.11.085.

[44] Oliver Grothe, Fabian Kächele, Mira Watermeyer, Analyzing Europe's biggest offshore wind farms: A data set with 40 years of hourly wind speeds and electricity production, Energies (ISSN: 1996-1073) 15 (5) (2022) http://dx.doi.org/10.3390/en15051700.

[45] Gorm B. Andresen, Rolando A. Rodriguez, Sarah Becker, Martin Greiner, The potential for arbitrage of wind and solar surplus power in Denmark, Energy (ISSN: 0360-5442) 76 (2014) 49–58, http://dx.doi.org/10.1016/j.energy.2014.03.033.

[46] Gorm B. Andresen, Anders A. Søndergaard, Martin Greiner, Validation of Danish wind time series from a new global renewable energy atlas for energy system analysis, Energy (ISSN: 0360-5442) 93 (2015) 1074–1088, http://dx.doi.org/10.1016/j.energy.2015.09.071.

[47] Stefan Pfenninger, Iain Staffell, Renewables.ninja, 2024, URL https://www.renewables.ninja/. (Accessed 14 October 2024).

[48] Michele M. Rienecker, Max J. Suarez, Ronald Gelaro, Ricardo Todling, Julio Bacmeister, Emily Liu, Michael G. Bosilovich, Siegfried D. Schubert, Lawrence Takacs, Gi-Kong Kim, Stephen Bloom, Junye Chen, Douglas Collins, Austin Conaty, Arlindo da Silva, Wei Gu, Joanna Joiner, Randal D. Koster, Robert Lucchesi, Andrea Molod, Tommy Owens, Steven Pawson, Philip Pegion, Christopher R. Redder, Rolf Reichle, Franklin R. Robertson, Albert G. Ruddick, Meta Sienkiewicz, Jack Woollen, Merra: Nasa's modern-era retrospective analysis for research and applications, J. Clim. 24 (14) (2011) 3624–3648, http://dx.doi.org/10.1175/JCLI-D-11-00015.1, URL https://journals.ametsoc.org/view/journals/clim/24/14/jcli-d-11-00015.1.

[49] Tue V. Jensen, Pierre Pinson, RE-Europe, a large-scale dataset for modeling a highly renewable European electricity system, Sci. Data 4 (1) (2017) 170175, http://dx.doi.org/10.1038/sdata.2017.175.

[50] Neil Hutcheon, Janusz W. Bialek, Updated and validated power flow model of the main continental European transmission network, in: 2013 IEEE Grenoble Conference, 2013, pp. 1–5, http://dx.doi.org/10.1109/PTC.2013.6652178.

[51] Tue V. Jensen, Hugo de Sevin, Martin Greiner, Pierre Pinson, The RE-Europe data set, 2017, http://dx.doi.org/10.5281/zenodo.999150.

[52] H. Hersbach, B. Bell, P. Berrisford, G. Biavati, A. Horányi, J. Muñoz Sabater, J. Nicolas, C. Peubey, R. Radu, I. Rozum, D. Schepers, A. Simmons, C. Soci, D. Dee, J.-N. Thépaut, ERA5 hourly data on single levels from 1979 to present. Copernicus climate change service (C3S) climate data store (CDS), 2018, Accessed on 15 November 2022.

[53] ENTSO-E Transparency Platform, Actual generation per production type, 2023, URL https://transparency.entsoe.eu/. (Accessed 13 January 2023).

[54] Soteris A. Kalogirou, Solar Energy Engineering: Processes and Systems, second ed., Academic Press, Boston, ISBN: 978-0-12-397270-5, 2014, http://dx.doi.org/10.1016/C2011-0-07038-2.

[55] J. Duffie, W. Beckmann, Solar Engineering of Thermal Processes, third ed., John Wiley and Sons, New Jersey, 2006.

[56] Spencer J.W., Fourier series representation of the position of the sun, Search 2 (5) (1971) 172+.

[57] Frank Kreith, Jan F. Kreider, Principles of Solar Engineering, in: Series in Thermal and Fluids Engineering, Hemisphere Publ. Corp., Washington, DC, ISBN: 0070354766, 1978, [u.a.].

[58] D.T. Reindl, W.A. Beckman, J.A. Duffie, Evaluation of hourly tilted surface radiation models, Sol. Energy (ISSN: 0038-092X) 45 (1) (1990) 9–17, http://dx.doi.org/10.1016/0038-092X(90)90061-G.

[59] D.T. Reindl, W.A. Beckman, J.A. Duffie, Diffuse fraction correlations, Sol. Energy (ISSN: 0038-092X) 45 (1) (1990) 1–7, http://dx.doi.org/10.1016/0038-092X(90)90060-P.

[60] Wilhelm Durisch, Dierk Tille, A. Wörz, Waltraud Plapp, Characterisation of photovoltaic generators, Appl. Energy (ISSN: 0306-2619) 65 (1) (2000) 273–284, http://dx.doi.org/10.1016/S0306-2619(99)00115-4.

[61] Hans Georg Beyer, Gerd Heilscher, Stefan Bofinger, A robust model for the MPP performance of different types of PV-modules applied for the performance check of grid connected systems, EuroSun (2004).

[62] Oliver Grothe, Felix Müsgens, The influence of spatial effects on wind power revenues under direct marketing rules, Energy Policy (ISSN: 0301-4215) 58 (2013) 237–247, http://dx.doi.org/10.1016/j.enpol.2013.03.004.

[63] Warren Katzenstein, Emily Fertig, Jay Apt, The variability of interconnected wind plants, Energy Policy (ISSN: 0301-4215) 38 (8) (2010) 4400–4410, http://dx.doi.org/10.1016/j.enpol.2010.03.069.

[64] John H. Seinfeld, Spyros N. Pandis, Atmospheric Chemistry and Physics: From Air Pollution to Climate Change, third ed., Wiley, ISBN: 978-1-118-94740-1, 2016.

[65] Stefan Emis, Wind Energy Meteorology, second ed., Springer Nature, ISBN: 978-3-319-72859-9, 2018, http://dx.doi.org/10.1007/978-3-319-72859-9.

[66] Irina Sandu, Ayrton Zadra, Nils Wedi, Impact of orographic drag on forecast skill, 2017, URL https://www.ecmwf.int/en/newsletter/150/meteorology/impact-orographic-drag-forecast-skill. (Accessed 09 October 2024).

[67] M. Dörenkämper, B.T. Olsen, B. Witha, A.N. Hahmann, N.N. Davis, J. Barcons, Y. Ezber, E. García-Bustamante, J.F. González-Rouco, J. Navarro, M. Sastre-Marugán, W. Trei Sīle, M. Žagar, J. Badger, J. Gottschall, J. Sanz Rodrigo, J. Mann, The making of the new european wind atlas – part 2: Production and evaluation, Geosci. Model Dev. 13 (10) (2020) 5079–5102, http://dx.doi.org/10.5194/gmd-13-5079-2020, URL https://gmd.copernicus.org/articles/13/5079/2020.

[68] Juan Pablo Murcia, Matti Juhani Koivisto, Graziela Luzia, Bjarke T. Olsen, Andrea N. Hahmann, Poul Ejnar Sørensen, Magnus Als, Validation of european-scale simulated wind speed and wind generation time series, Appl. Energy (ISSN: 0306-2619) 305 (2022) 117794, http://dx.doi.org/10.1016/j.apenergy.2021.117794, URL https://www.sciencedirect.com/science/article/pii/S0306261921011296.

[69] Cristina L. Archer, Mark Z. Jacobson, Supplying baseload power and reducing transmission requirements by interconnecting wind farms, J. Appl. Meteorol. Climatol. 46 (11) (2007) 1701–1717, http://dx.doi.org/10.1175/2007JAMC1538.1.

[70] Trevor Hastie, Robert Tibshirani, Jerome Friedman, The Elements of Statistical Learning, in: Springer Series in Statistics, Springer New York Inc., New York, NY, USA, 2001.

[71] Hui Zou, Trevor Hastie, Regularization and variable selection via the elastic net, J. R. Stat. Soc. Ser. B Stat. Methodol. 67 (2) (2005) 301–320, http://dx.doi.org/10.1111/j.1467-9868.2005.00503.x.

[72] Arthur E. Hoerl, Robert W. Kennard, Ridge regression: Biased estimation for nonorthogonal problems, Technometrics 42 (1) (2000) 80–86, http://dx.doi.org/10.1080/00401706.2000.10485983.

[73] Federal Office of Justice and Federal Ministry of Justice, Gesetz für den ausbau erneuerbarer energien (Erneuerbare-Energien-Gesetz - EEG 2021), 2021.

[74] Bundesnetzagentur für Elektrizität, Gas, Telekommunikation, Post und Eisenbahnen and bundeskartellamt. Monitoringbericht 2021, 2022, URL https://www.bundesnetzagentur.de/SharedDocs/Mediathek/Monitoringberichte/Monitoringbericht_Energie2021.pdf?__blob=publicationFile&v=2. (Accessed 24 February 2023).

[75] G. Luzia, A.N. Hahmann, M.J. Koivisto, Evaluating the mesoscale spatio-temporal variability in simulated wind speed time series over Northern Europe, Wind Energy Sci. 7 (6) (2022) 2255–2270, http://dx.doi.org/10.5194/wes-7-2255-2022, URL https://wes.copernicus.org/articles/7/2255/2022.

[76] ENTSO-E Transparency Platform, Installed capacity per production type, 2023, URL https://transparency.entsoe.eu/. (Accessed 24 February 2023).

[77] International Renewable Energy Agency, IRENASTAT Online Data Query Tool, 2023, URL https://www.irena.org/Data/Downloads/IRENASTAT. (Accessed 17 February 2023).

[78] 50Hertz Transmission GmbH, Amprion GmbH, TenneT T.S.O. GmbH, TransnetBW GmbH, Szenariorahmen zum netzentwicklungsplan strom 2037 mit ausblick 2045, version 2023, 2023, URL https://www.netzausbau.de/SharedDocs/Downloads/DE/Bedarfsermittlung/2037/SR/Szenariorahmen_2037_Entwurf.pdf?__blob=publicationFile. (Accessed 24 February 2023).

[79] TenneT TSO GmbH, Project suedlink, 2023, URL https://www.tennet.eu/de/de/projekte/suedlink. (Accessed 24 February 2023).

[80] TransnetBW GmbH, Project suedlink, 2023, URL https://www.transnetbw.de/de/netzentwicklung/projekte/suedlink. (Accessed 24 February 2023).

[81] Federal Office of Justice and Federal Ministry of Justice, Gesetz über den bundesbedarfsplan (Bundesbedarfsplangesetz - BBPlG), 2022, URL http://www.gesetze-im-internet.de/bbplg/BJNR254310013.html. Accessed on 24 February 2023.

[82] Bundesnetzagentur, Marktstammdatenregister (MaStR) – core energy market data register, 2019, URL https://www.marktstammdatenregister.de/MaStR. (Accessed 15 November 2022).